東北大学機関リポジトリ
TOUR
Tohoku University Repository

Observation of the local density of states of MoS2 nanosheets using atomic force microscope-assisted tunneling spectroscopy

著者	Amin Vakhshouri
学位授与機関	Tohoku University
学位授与番号	11301甲第16157号
URL	http://hdl.handle.net/10097/60436

Observation of the local density of states of MoS_2 nanosheets using atomic force microscope-assisted tunneling spectroscopy

AMIN VAKHSHOURI

GRADUATE SCHOOL OF SCIENCE, DEPARTMENT OF PHYSICS

TOHOKU UNIVERSITY

IN PARTIAL FULFILLMENT OF THE REQUIREMENTS
FOR THE DEGREE OF
DOCTOR OF PHILOSOPHY
IN THE SUBJECT OF

PHYSICS

I would like to dedicate this thesis to my loving parents ...

Acknowledgements

I would like express my gratitude to my adviser, Prof. Yoshiro Hirayama, from whom I have learned a lot during the graduate school years. His brilliant ideas and deep insights in both theoretical and experimental physics beside his modesty and leadership intelligence have been always inspiring me. I would also like to thank Dr. Katsushi Hashimoto who undertook to act as my subgroup leader despite his many other academic commitments. His hard working and friendly character have been motivating me during last the six years.

Research staffs and students in our group have been so supportive to me. Dr. H. Liu, Dr. K.Yang and Dr. K.Akiba have always guided me to the important points in my research during the group seminars. I am thankful to Dr. T. Tomimatsu, Dr. S. Miyamoto and Dr. M. H. Fauzi with whom I had lots of fun discussions about life and research. Without the other graduate students: S. Shirai, K. Yamaguchi, N. Moore, M. F. Sahdan and Y. Horigome the atmosphere in the lab would certainly be less enthusiastic. During my research, I have received lots of support from K. Nagase and K. Sato for the technical aspects.

I am thankful to my uncle and his family whose presence in Japan has been a great source of emotion for me. Among my best friends are P. Ayria, R. Ranjbar, A. Zamani and S. Kumagai who have been so supportive to me during last years.

I am indebted to my parents who have always encouraged me to pursue my gaols.

Abstract

Molybdenum disulphide, a transition-metal dichalcogenide-based two-dimensional atomic crystal, has unique electronics properties which can vary locally due to numerous factors such as the number of atomic layers and strain. To understand these local changes in electronic structures, this thesis presents results of local density of states (LDOS) on MoS_2 nanosheets measured by atomic force-assisted scanning tunneling spectroscopy (STS) under ambient conditions. This developed technique together with the combined atomic force/tunneling microscope (AFM/STM) enable fast access to a desire area on the sample as well as stable spectroscopy measurements by compensating for the vertical thermal drift.

The first part of the thesis discusses a technique to use a cantilever-based AFM as an alternative AFM/STM. Also a method of AFM-assisted STS is proposed which shows its merits for STS on layered material devices in ambient conditions. The second part of the thesis, presents the observation of LDOS of the MoS_2 nanosheets deposited on Au substrates, and their spatial dependency.

Contents

List of Figures

Chapter 1

Introduction

Recent breakthrough in fabrication of graphene, i.e. mechanical exfoliation method [1], has paved the way for investigation of other layered materials including molybdenum disulfide (MoS_2). Unlike graphene, MoS_2 has an intrinsic bandgap [2] which is critical for device application. MoS_2 nanosheets have extensively been studied in the recent years using the transport technique. For instance, the transport measurement on a monolayer MoS_2-based transistor has demonstrated high current on/off ratio ($\sim 10^8$) and a sharp subthreshold slope of 74 mV/dec reflecting low energy dissipation [3]. Higher mobility ($\sim$ 700 cm^2/V.s) [4] than that of the monolayer MoS_2 ($\sim$ 200 cm^2/V.s) [3] has been achieved in nanosheets (multilayer) owing to the effective screening of the substrate impact, i.e. gate oxide. This mobility is also larger than mobility of the bandgap-engineered graphene, i.e. nanoribbon, which is about 200 cm^2/V.s [5] These features make MoS_2 nanosheet an attractive replacement for silicon$-$based logic devices. In the transport techniques, one measures the average electronic properties of the material that is typically a few micrometer (semiconductor channel). Also, the metallic contacts and the back gate oxide layer can affect the electronic properties.

Unlike the transport techniques, local probe measurements allow one to measure properties of the material on the sub$-$nanometer scale. A good example is scanning tunneling microscope (STM) that operates by means of a quantum mechanical phenomenon, i.e., the tunneling effect [6]. One exceptional capability of STM is probing the local density of states (LDOS) and their spatial evolution using scanning tunneling spectroscopy (STS). Having a small working distance of

a few angstroms, STM becomes an inefficient and slow technique when the surface is not flat, and a large scan range is required to find a targeting area. This is the case for MoS_2 nanosheets obtained by mechanical exfoliation. Their typical thickness and width are a few nanometer and a few micrometer [7], respectively. An alternative technique, for navigating the tip toward the nanosheets, is the amplitude−modulated atomic force microscopy (AFM) [8]. In this method, a tip mounted at the end of the cantilever is oscillated above the surface, and the tip-sample distance is controlled by maintaining the constant oscillation amplitude. The amplitude can be tuned such that the tip−sample interaction forces dominant by the long-range van der Waals forces in an attractive regime. Under this condition, tip−sample distance ranges from a few angstroms to a few nanometres. Scanning capability with such a large tip-sample distances makes AFM a suitable tool for profiling surfaces with large corrugations.

In this thesis, I discuss the development of an AFM-assisted STS method that is suitable for the STS studying of the layered materials' nanosheets. This method is different from the traditional combined AFM/STM [9, 10]. These microscopes are designed to study the correlation between the atomic force and the tunneling current in atomic scales. For this reason, the simultaneous observation of the forces and current is of the interest. In order to achieve atomic resolution, the sophisticated facilities are needed to reach the ultra high vacuum (UHV) and low-temperature conditions. In addition, in typical AFM/STM, the small range scanners are used to reduce the noise level. However, the objective of this work is the investigation of the electronic properties of the MoS_2 nanosheets. Here, we utilize an AFM to locate the probe in the area of the interest on nanosheets and then switch to STM mode in order to perform tunneling spectroscopy. For this purpose, the large range scanners are favorable since the exfoliated nanosheets are a few micrometer in lateral size and are typically distributed tens of micrometers far from each other. In addition, the AFM-assisted STS is operating in ambient conditions that allow us to perform more efficient measurements because the procedure of the tip and sample changing is quicker than that of UHV systems. The experimental conditions, for performing AFM and STM imaging using a conductive cantilever, is determined.

In addition, we propose a method to counteract the vertical thermal (TD)

during the STS measurements. In this method, the AFM feedback is employed to keep the tip-sample separation constant. The advantage of this method over the previously reported technique [11] is that the tip-sample separation is actively adjusted and. The reported technique is based on the assumption that the TD rate is constant, and the tip position is varied constantly to compensate for the drift.

Finally, we employed the AFM-assisted method study the thickness, and spatial dependency of the doping behavior of the MoS_2 nanosheets. Majority of the transport measurements on MoS_2 have reported n−doping behavior [3, 12, 4, 13]. In contrast, the reported p−type is very rare [14]. In this work, we observed of the n-type for thinner nanosheets with the thickness less than 14 nm and the p-type behavior for nanosheets thicker than 14 nm.

This thesis is divided into five chapters;
Chapter 2 is a review of crystal and electronic structures of MoS_2, followed by a review of the principals of scanning probe microscopy methods.

Chapter 3 describes sample preparation methods used for MoS_2 nanosheets. The identification methods of nanosheets deposited on gold substrates (for STS measurements) using an optical microscope is included. In the last section, the results of the analysis of the samples and substrate surface are presented. The development of AFM-assisted STS is discussed in chapter 4. Consecutive AFM and STM imaging on the surface of graphite is demonstrated, and the performance of this microscope is discussed. The STS result on graphite that used as a reference sample obtained by the above−mentioned method is also presented.

The topic of chapter 5 is the implementation of the AFM−assisted STS for studying the electronic structures of MoS_2 nanosheets. The doping type in different nanosheets and the spatial mapping of local density of states are investigated.

The thesis is summarized in the final chapter.

Chapter 2

Properties of MoS_2 and Scanning Probe Microscopy

2.1 Molybdenum disulfide and its electrical properties

As the semiconductor industry is approaching the performance limit of the miniaturized electronic elements, 2D materials are getting considerable attentions to be a substitute for the current Si-based devices. One of the suitable candidates is molybdenum disulfide (MoS_2), a layered transition metal dichalcogenide semiconductor with unique electronic properties such as bandgap and low standby power [3, 2].

This 2D material has a graphene-like hexagonal structure formed by arrangement of Mo and S atoms. Single layer of MoS_2 include one layer of Mo sandwiched between two layers of S. These monolayers are stuck together by weak van der Waals forces. This weak forces interacting between the layers enable synthesis of multi or single layer using a number of techniques including micromechanical or liquid-based exfoliation methods [1, 15]. The unit cell of bulk 2H-MoS_2 contains 2 Mo and 4 S atoms coordinated in a triangular prismatic fashion. The stacking structure is AB type [Fig. 2.1 (b)]. The crystal structure is characterized by hexagonal lattice constants a, out-of-plane lattice constant c and the internal displacement parameter z = 0.12 [16] [see Fig. 2.1 (b)].

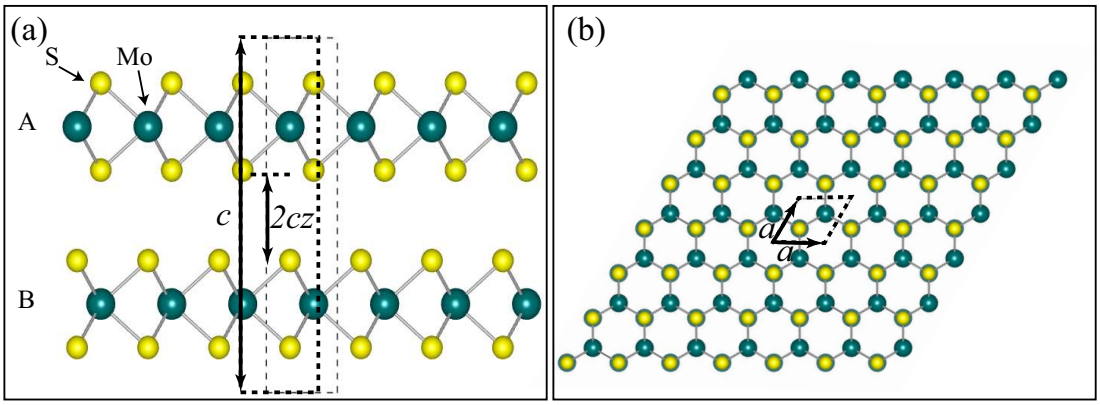

Figure 2.1: (a) Side view of a 2H-MoS_2 bulk. Dark and yellow spheres represent Mo and S atoms respectively. The unit cell marked by the dashed-line rectangle. Out-of-plane lattice constant c and displacement parameter z are indicated. (b) Top view of the lattice shown in (a). The unit cell (dashed line) and lattice constant a are displayed.

The bulk MoS_2 has an indirect bandgap ~ 1.3 eV. The valance band maximum locates at and Γ point in K$-$space while the conduction minimum is in the middle of the K and Γ points (see left diagram in Fig. 2.2). The indirect bandgap changes into direct bandgap of ~ 1.8 eV when MoS_2 is thinned down to a single layer. In this case, both valance band maximum and conduction band minimum occur at K point of the Brillouin zone [2, 17]. The calculated band structures show that electronic states at K and Γ points involves orbitals with different spatial distribution. Notably, conduction band states at the K point are composed of localized d orbitals at Mo atom sites. They have weak interlayer coupling since Mo atoms sandwiched in the middle of the S-Mo-S unit cell. However, states near the Γ point and the point of indirect bandgap originate from a linear combination of d orbitals of Mo atoms and p_z orbitals of S atoms. They have strong interlayer coupling and their energies depend on layer thickness [17]. The band structures of few layer of bulk and single layer MoS_2 are depicted in Fig. 2.2.

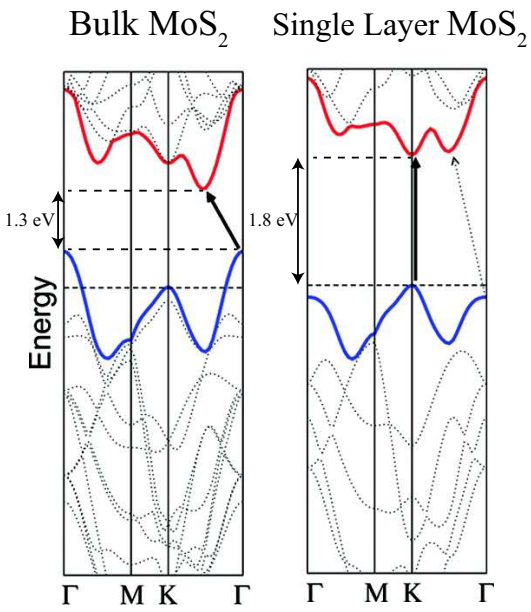

Figure 2.2: Left: The indirect bandgap of bulk MoS_2. The valance-band maximum and the conduction band minimum locate at Brillouin zone Γ and middle of $K\Gamma$ points respectively. Right: The change of bandgap occurs in the single layer MoS_2 at K point.Figure reproduced from reference [17].

2.2 Scanning tunneling microscopy

Electron, as an elementary particle, behaves as a wave-matter that permits the tunneling through an energy barrier between two surfaces. This so-called quantum tunneling phenomenon was first employed by Binnig and Rohrer [18] in order to image the surface of materials with atomic resolution. When two metals are brought near enough, (∼1nm), electrons from occupied states of the negatively biased surface (sample) tunnels into unoccupied states of the positively biased surface (tip). This is illustrated in an energy band diagrams in Fig. 2.3. The tunneling current I_t, can be derived by using Fermis golden rule of first-order time-dependent perturbation theory [19, 20, 21]:

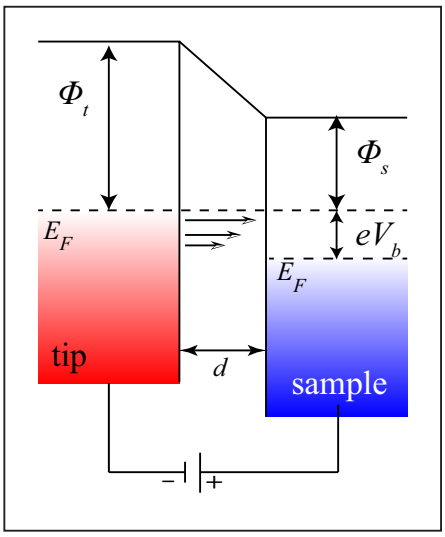

Figure 2.3: Schematics of the tunneling junction between the tip and the sample. Both tip and the sample are assumed to be metallic with constant DOS. The Fermi energy of the electron in the tip is shifted upward due to negative bias voltage. Arrows pointing to the sample near the Fermi energy E_F indicate the tunneling electrons from the tip to the sample.

$$I_t = \frac{4\pi e}{\hbar} \int_{-\infty}^{\infty} |M|^2 \, \rho_s(E_F - eV_b + E)\rho_t(E_F + E) \times [f(E_F - eV_b + E) - f(E_F + E)]dE \tag{2.1}$$

where M is the tunneling matrix, ρ_s and ρ_t are the density of states (DOS)

of the sample and the tip, $f(E)$ is the Fermi function, e is electron charge, $\hbar$ is reduced Planck constant and V_b is the tip-sample bias. By assuming a simple square tunnel barrier and exponential decay of the wavefunctions, the matrix M, can be written as:

$$\left|M^2\right| \propto exp(\frac{-2d}{\hbar}\sqrt{2m\phi}) \tag{2.2}$$

Here, m is the electron mass, d is the separation of the tip and sample, and ϕ is the effective barrier height. The latter is the average of tip and sample work functions: $(\phi_t+\phi_s)/2$. Plugging Eq. 2.2 in Eq. 2.1 one can write the tunneling current as:

$$I_t \propto exp(\frac{-2d}{\hbar}) \tag{2.3}$$

The exponential decay of current, with increasing the tip-sample separation, is the basis of the scanning tunneling microscope (STM). Therefore, by keeping the tunneling current constant using a feedback loop system, tip closely follows the sample corrugation while scanning across the surface. The contour maps obtained in this scanning mode (constant current mode) are often referred to the topographic images of the sample surface. However, the better interpretation of them is the contour map of constant charge densities [20].

2.3 Tunneling spectroscopy

Besides the topography, STM is capable of probing DOS of the sample. By assuming a constant DOS in energy for the metallic tip and by taking the derivative of I_t in Eq. 2.1 with respect V_b, we obtain:

$$\frac{dI_t}{dV_b} \propto \rho_s(x, y, eV_b) \tag{2.4}$$

The DOS also varies as a function of position (x, y). Thus by changing the location of the tip and the bias voltage, the so-called local density of states (LDOS) at different energies is observable. A common way to perform tunneling spectroscopy is to scan the tip to the point of interest using STM feedback. Afterward, disabling the feedback loop and sweeping V_b while recording the I_t.

The LDOS is measurable directly using lock-in technique in which modulated ΔV_b added to the V_b and the resulting ΔI_t is detected. Another way to obtain LDOS is to numerical differentiation of the $I_t(V_b)$ curve.

2.4 Atomic force microscopy

Soon after the invention of STM, atomic force microscope (AFM) was developed by Binnig *et al*. [22]. The core idea behind the first AFM was using the sensitivity of STM to measure the deflection of a cantilever q in angstrom accuracy. In other words, the force sensor was an STM. However, a stable configuration of STM tip on a cantilever cannot easily be achieved and, therefore, more efficient methods to monitor q, such as optical-based techniques, were developed [23]. In this work, the deflection is measured by using an optical-base technique.

The operation of AFM is categorized into two main modes: contact (static) and non-contact (dynamic). In contact AFM mode, the tip makes physical contact with the sample. As the scanner traces the tip over the sample surface, the interaction forces cause the cantilever to bend. This bending can be detected, for instance using optical−based technique. In one schemes of optical methods, the laser beam is focused on the end of the cantilever where the tip is attached. The reflected laser beam from the cantilever is detected by a photodiode. The change in the position of the laser beam spot (measured by the photodiode) is proportional to the variation of the q. The feedback loop in contact mode maintains the constant q. As a result, the variation of the z−piezo is interpreted as the surface corrugations [see Fig. 2.4 (a)].

In non−contact mode [8, 24, 25], the cantilever is deliberately oscillated by an actuator at a fixed amplitude and frequency. Depending on the usage, the feedback loop keeps the oscillation amplitude (AM-AFM), frequency (FM-AFM) or phase (or all of them) constant. For example, AM-mode is proper for scanning the rough surfaces and FM-mode has a higher sensitivity and for this reason it is usually used for high-resolution AFMs. The schematic of non-contact mode is shown in Fig. 2.4 (b).

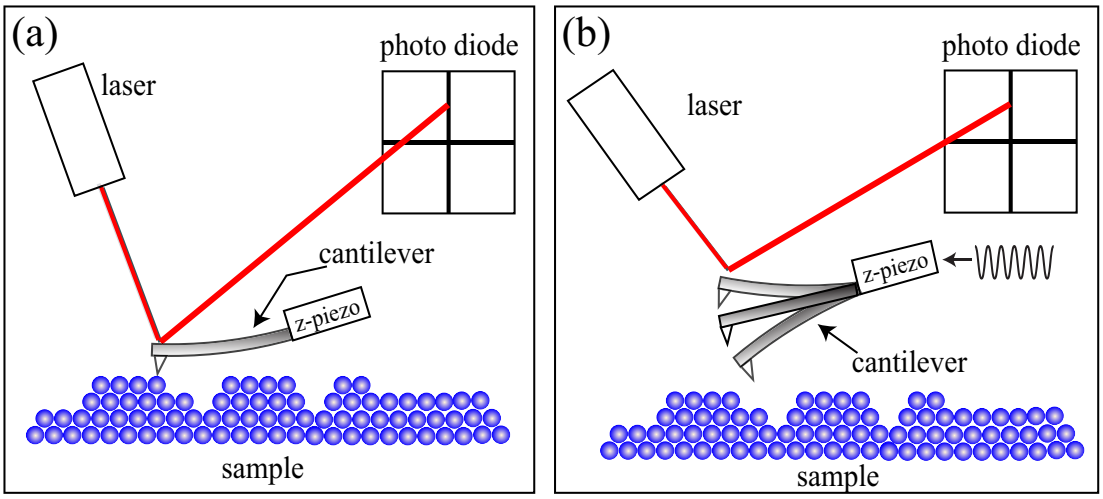

Figure 2.4: Schematic image of the operational modes of contact and non− contact. (a) In contact mode, the force (deflection) is kept constant. (b) In non− contact operational mode, the cantilever is oscillated above the sample, and the oscillation parameters such as amplitude, frequency, and phase can be used as a feedback input.

2.5 Force regimes

The interacting forces between the tip and the sample, unlike the tunneling current, has a non-monotonic dependence on the tip-sample separation r. As the tip and sample are brought together, they first weakly attract each other via long-range van der Waals force F_{vdW} .The F_{vdW} is a combination of several forces such as electrostatics and the universal intermolecular forces, i.e. London or dispersion forces [26]. Another type of forces that usually present in contact AFM is capillary force that is due to the thin water layer often present in an ambient environment. The attraction increases until the electron clouds of the tip and sample start to overlap. As a result, tip and sample repel each other electrostatically. The effective range of the several forces is illustrated in Fig. 2.5 (a). The repulsive regime is defined in such close tip−sample separations and the forces are short-range in this regime. When the total force becomes positive, i.e. repulsive, the atoms are in contact. Note that, in non−contact mode, the oscillation of the cantilever can be tunned in such a way that either attractive or repulsive regime

be probed.

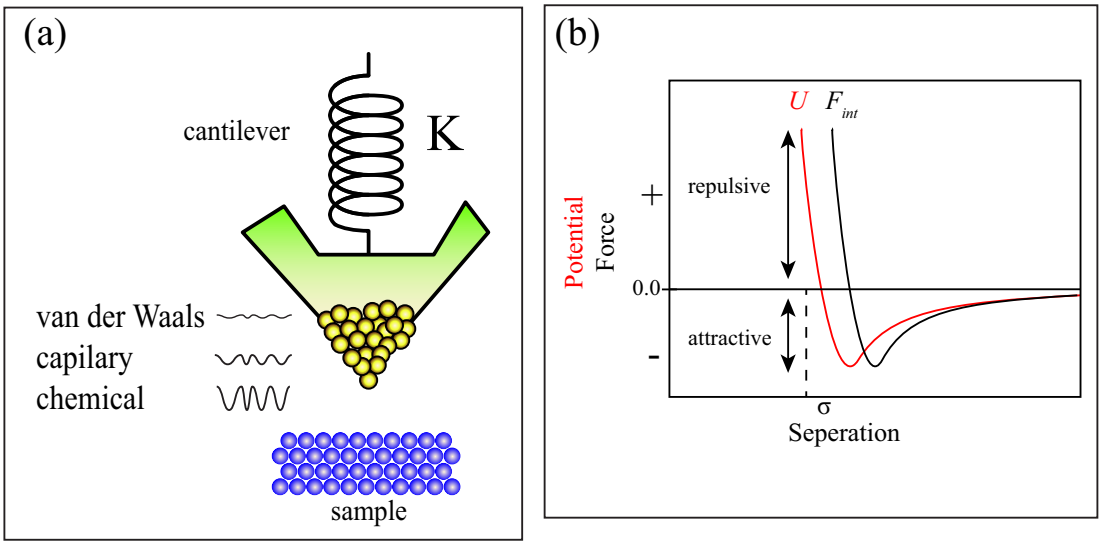

Figure 2.5: (a) Illustration of the spring model of the cantilever with the spring constant of K. Surface corrugations measured at different tip−sample distances are schematically drawn with the corresponding interaction. (b) Lennard-Jones Potential (red), interaction forces (black). The repulsive and attractive forces regime are indicated by arrows. At the separation of σ the potential is zero.

The total potential between the tip and the sample can be modeled by Lennard-Jones interatomic potential:

$$U(r) = 4U_0 \left[\left(\frac{\sigma}{r}\right)^{12} - \left(\frac{\sigma}{r}\right)^{6} \right] \tag{2.5}$$

Where, U_0 is depth of potential and σ is the separation at which $U = 0.$, i.e. the attractive and repulsive forces compensate each other. The potential in the attractive regime varies as $1/r^6$ while the potential is in the form of $1/r^{12}$ in a repulsive regime. The schematic of the total potential and force (i.e. the gradient of the potential) are illustrated in Fig. 2.5 (b). By taking into account the mechanical model (mass-spring) of the cantilever [see Fig. 2.5 (a)], the relationship between q and the tip-sample interaction forces F_{int} can be written as:

$$F_{int} = -K\Delta q \tag{2.6}$$

where, K is the cantilever spring constant. As mentioned in the previous section, the force exerted to the cantilever can be detected by monitoring the deflection, i.e. q, of the cantilever.

The extension and compression of the spring indicate the effect of attractive and repulsive forces respectively. These two situation can be distinguished from the sign of the deflection if the free-force case is calibrated to zero by setting the laser spot to the middle of the photodiode. In the case of attraction forces, the deflection is negative and the repulsive forces induce positive deflection.

2.6 Conventional combined AFM/STM vs. AFM-assisted STS

The motivation behind the combined AFM/STM microscopes is the investigation of the correlation between the tip-sample interaction forces (F) and the tunneling current (I_t) with atomic resolution. In the following, the requirements, for obtaining atomic resolution images by AFM, are discussed. However as it will be discussed at the end of this section, the conventional combined AFM/STMs are not suitable for electronic studying of MoS_2 nanosheets. As a result, in this work, the proper combination of the AFM and STM, which fulfills the requirements for investigation of the nanosheets is proposed.

2.6.1 Conventional combined AFM/STM

The development of such a combined AFM/STM was first achieved by utilizing a STM tip as a force detector [9, 27] similar to the method used by Binnig et. al. for the first AFM [22]. In this method, as shown in Fig. 2.6, the deflection of the cantilever was detected by tunneling current between the tunneling tip (Pt−Ir) and the conductive cantilever (W−lever). The STM signal was directly measured by monitoring the tunneling current I_t flowing between the sample surface and the tip of the cantilever with the voltage V_b. This configuration of STM tip and the AFM cantilever makes the operation of AFM/ATM rather complicated and inefficient. For example, it is quite difficult to position the tip close to a cantilever. Also, the STM tip exerts force to the cantilever that makes it difficult to measure

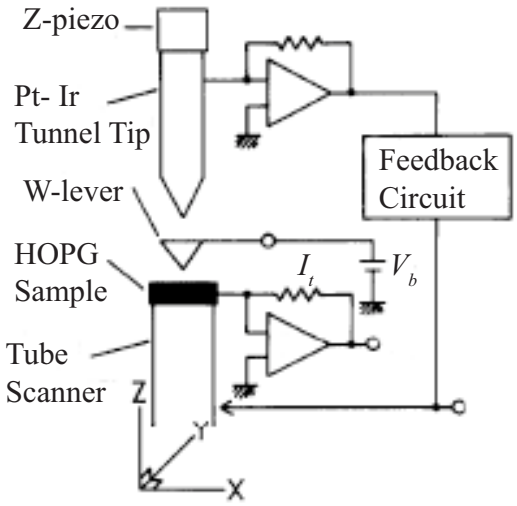

Figure 2.6: Schematic diagram of the first combined AFM/STM. The force sensing is done by an STM tip. Adapted from ref. [27]

the pure tip−sample interaction forces. Moreover, simultaneous AFM and STM images of graphite were obtained only when the tip and the sample where in contact, i.e. repulsive force regime, and F exceeded $\sim 1.1 \times 10^{-6}$ N. This large amount of force might cause damage to the sample during the scanning. Despite the atomic resolution achieved in contact mode, the absence of the atomic defects implies that the contact area of the tip−sample should be larger than the size of a single atom [28]. This is shown in Fig. 2.7. For this reason, the true atomic resolution cannot be achieved in contact mode.

The non−contact imaging was achieved after the development of force sensing methods. After the early design of the AFM/STM, the force sensing using STM replaced by optical methods, e.g., beam-bounce, and electrical methods, e.g., piezoelectric. In the former method, the deflection of the cantilever is measured by a change in the angle of the laser beam bounced back from the top surface of the cantilever. In the latter method, the cantilever is made of a piezoelectric material, and its bending is measured by the change in the voltage of the pieozoelectric. Thanks to these methods, a single cantilever could be used for detection of both F and I_t and more importantly the true atomic resolution for AFM was achieved.

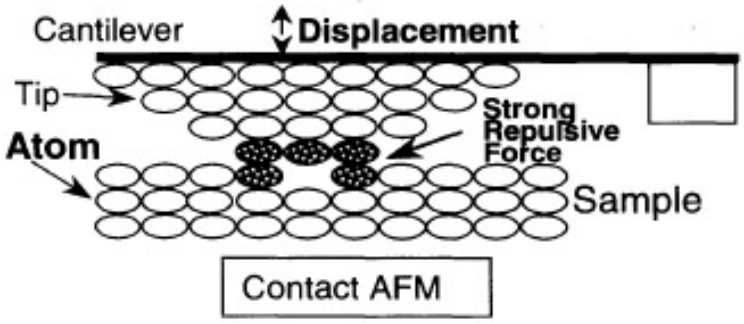

Figure 2.7: Schematic model of contact mode AFM shows that contact mode AFM has a large contact area. Adapted from ref. [28].

Recent AFM/STMs are typically operating in ultrahigh vacuum (UHV) [10] because this condition is particularly necessary for studying the surfaces of the solids that are unstable in ambient conditions. Also, UHV conditions lead to higher force sensitivity. Because the quality factor (Q) of the cantilever resonant which is typically a few hundred in air can reach hundreds of thousands in vacuum [28] since the oscillation damping vanishes in UHV. However, compared with microscopes operating under ambient conditions, the demerit of UHV systems is that it requires sophisticated vacuum equipments that hinder the process of the sample and/tip changing.

Another requirement, for achieving atomic resolution, is the low noise in the lateral position (X, Y) signals. This condition is usually satisfied by using small$-$range $X-Y$ piezoelectric tubes. Common problems with piezoelectric actuators include non-linearity which is more pronounced when scanners are run in an open-loop fashion, i.e. the scan is performed by applying a linear voltage ramp to the piezos and the effective motion is measured. Because of the non-linearity of the piezos in the range of 10 of the full scan range, this mode might lead to a non-equidistant net of data. This means that the achieved resolution is not uniform over the whole image. For larger scan areas ($10-100$ μm), the nonlinearity becomes more noticeable due to the high fields required to drive the scanner [20]. In contrast, scanning in a closed$-$loop fashion allows one to use the full range of the scanner and measuring the absolute value of the piezos. This can

be done by, for instance, capacitive or magnetic−based sensors. These sensors require additional space in the design of the AFM or STM and, as a result, they are not proper for high-resolution microscopes where the size should be minimized to achieve less mechanical noise. For this reason, in typical AFM/STM small range scanners working in open−loop mode is favorable.

2.6.2 Thermal drift and the solutions

One of the challenges, in scanning probe techniques, is the effect of thermal drift (TD) on the imaging and spectroscopy. The TD can cause by the thermal expansion of any component of microscope such as scanner piezos, sample stage or the tip holder. The effect of the lateral TD, i.e. in X and Y directions, translated as distortions in the images. The effects of TD on spectroscopy data can be strong since the required acquisition time is longer than typical scanning. In the case of tunneling spectroscopy, the tunneling junction, i.e. the tip−sample distance, is not controlled by the STM feedback and therefore the vertical TD can cause artifacts such as collapse of the tunneling junction and eventually a tip crash. One solution to this problem is performing measurements at low temperatures as employed by Hembacher et. al. [10]. In the mentioned report, the thermal drift rate minimized down to $\sim$ 20 pm/h when the microscope immersed in the at liquid Helium bath with the base temperature of 4.2 K. The drawback of low temperature measurements is the slow cooling down process. In addition, the scanning speed should be reduced in order to avoid the temperature increase.

As for room temperature microscopes, the TD rates are about few nm/h that is two orders of magnitudes more than that of the low-temperature systems. One proposed solution [11] for the TD compensation at room temperature is as follows. First the drift rates in all X, Y and Z directions are measured. Second the scanners are derived in the opposite direction to that movement caused by of the drift at the same rate, i.e. velocity. In this solution, it is assumed that the drift rates are constant over the time between the first and the second steps. Meaning that this method is a passive compensation technique. Although, the assumption of the constant drift rates can be valid within few minutes, it cannot be extended to the time span of few hours since the temperature does fluctuate

and affect the TD rates. As a result, in the mentioned method, one needs to measure the drift rates before each experiment. In this work we propose an active compensation for the TD during the spectroscopy measurements using the AFM feedback. Here, active means the compensation does not depend on the TD rate and the adjustment of the tip's vertical position is not performed at a constant rate but it depends on the tip-sample forces which is sensitive to the tip-sample gap. Therefore, using this method one does not need to measure the drift rate before each measurement.

2.6.3 AFM−assisted scanning tunneling spectroscopy

The tipsample distance in STM is limited to the decay length of tunneling current, which is of the order of a few angstroms. Small tip-sample separation makes STM a near-sighted technique that hampers the navigation of the tip toward the desired scanning area. Particularly in STS studying of the micron size flakes of graphene or other layered materials, e.g. MoS_2. A variety of approaches to this issue has been reported such as topography guiding [29]. This process requires several small size images, and since the typical dynamic range of STM scanners are limited (∼100 nm), the navigating time increases drastically which makes this technique inefficient. Another solution is capacitive method [30, 31] in which small samples can be located by measuring the capacitive current between tip and sample while the tip is hovering far (out of tunneling regime) from the sample. However, this method does is insensitive to small structures within the sample area such as corrugations. In contrast, AFM is capable of sensing long-range (several anometers) tipsample interaction forces, i.e., van der Waals forces. In AM-mode [8] which is a non-contact method, the tipsample separation can reach nanometer scale, one order of magnitude larger than for STM [28]. Thus by performing AM-AFM one can image a non−atomically flat surface without tip crash faster than when using STM. Besides, it provides direct topography of the sample.

In addition to scanning the non−flat regions we need large scan ranges in order to locate the nanosheets. This is because the nanosheets are not homogeneously distributed on the substrate and are located few tens of μm far from

each other. We take the advantage of a commercial available AFM (Asylum research, MFP-3D, CA, USA) where large range scanners are used in closed−loop mode. By modifying the control software and adding an external amplifier, we added the STM and STS functions to the microscope. In addition, the required condition for performing AFM and STM with cantilevers, i.e. using cantilevers with high enough spring constant, was determined. The large scanning area of our system eases finding and identifying a particular region of interest. This can sometimes be difficult with conventional AFM/STMs, since they are typically based on piezo tubes with limited scan range, especially at low temperatures. Often, conventional AFM/STMs are even completely lacking lateral positioning capabilities over macroscopic ranges.

In addition, thanks to chemical stability of the MoS_2 nanosheets, we can perform AFM and STS measurements in air which simplifies the sample/tip changing process compared with UHV systems.

Another feature of our AFM−assisted STS is the thermal drift compensation in the vertical direction. In this method, the static AFM signal, i.e. the deflection, is used as a feedback signal for the tunneling spectroscopy. Using this method, the tip−sample gap can be kept constant for tens of seconds which enables the detection of STS signal using lock−in technique. The advantage of this method over the previously reported technique [11] is that additional measurements for estimating the thermal drift rate is not necessary, since the AFM feedback actively compensates the vertical drift (even though the rate changes by temperature fluctuations). This method will be discussed in more detail in chapter 4.

In summary, the trend of the development of the conventional AFM/STMs is to investigating the correlation between the forces and the electronic properties of the materials at atomic resolution. To this end, performing measurements in UHV and low-temperature conditions is necessary. Additionally, the scanning range should be limited to small values. As a result, such systems are proper for studying the atomically flat surfaces where the whole area is covered with the same material and therefore approaching the tip to a particular area is not concerned. However, in this work, we are focusing on the electronic properties of the MoS_2 nanosheets that are unevenly distributed on the substrate and the selective access to them is required. Therefore, we take the advantage of the AFM

to have a quick and accurate access to a desire nanosheet and then switching into STM mode for performing tunneling spectroscopy. Additionally, taking into account that MoS_2 is chemically inert in air, our system operates in ambient conditions. This allows us to conduct more measurements more efficiently as the process of the tip and sample changing is much faster than that in UHV and low-temperature systems. Also, we propose a method to compensate thermal drift effect during spectroscopy measurements.

Chapter 3

Materials and Methods

3.1 Sample fabrication

3.1.1 Graphite

The graphite sample used for AFM/STM and STS measurements is commercially available HOPG (SPI 476HP-AB) bulk crystal with the dimension of 5 × 5 × 1 mm^3. The same sample used for the calibration of the spring constant of the cantilevers. The sample surface was cleaved by a scotch tape prior to the measurements to obtain a fresh surface. The HOPG sample mounted on microscope glass slide using silver paste (SPI). It then, electrically biased near the edge of the sample via a flexible coaxial cable (LakeShore CC-SC-50) [see Fig.3.1(a)].

3.1.2 Gold substrates

The Au films deposited on glass are very common substrate for STM and STS measurements. Since they provide a conductive substrate with a metallic electronic structure that can be used as a reference. That is the constant density of states as a function of energy. We used two different Au substrates for the deposition of MoS_2 nanosheets:

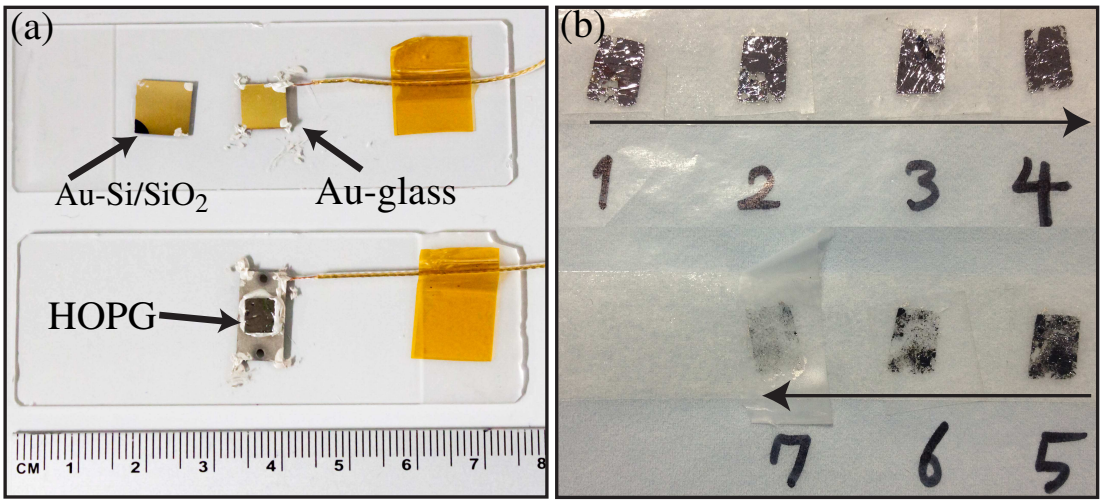

Figure 3.1: (a) Electrically wired HOPG and Au samples mounted on glass slides. (b) The procedure of micromechanical exfoliation using a scotch tape. The thinner MoS_2 nanosheets can be obtained by repeating the peeling process.

3.1.2.1 Au (111) film on glass

One type of substrates is typical Au films deposited on 8 mm × 8 mm glass that are commercially available (Gold arrandee). Au (111) surfaces prepared as follows: First, they were washed in acetone, Isopropanol and distillated water for 5, 3 and 1 minute respectively. Second, they were flame annealed with the expected maximum temperature of ∼1400 ° C for three times with the interval of 30 seconds. For STS measurements, these conductive substrates were used.

3.1.2.2 Ti/Au on Si/SiO_2

Another type of substrate is Ti/Au film deposited on Si/SiO_2 (n-type doped Si with thickness of SiO_2= 285 nm ,Umesato-electronics) by an e-beam evaporator (ANELVI P-011CCC) operating under high vacuum conditions ($P < 1.5 \times 10^{-7}$ Torr). Thickness of Au and Ti are 250 and 20 nm. The Si/SiO_2 wafers washed in a similar way as Au/glass samples. They also exposed to O_2 plasma (SAMCO FA-1) for 1 minute with the flow rate of 20 ml/min and RF power of 20 W, prior to metal deposition. As will be discussed later in this chapter, the surfaces show different roughness.

3.1.3 Preparing MoS_2 nanosheets

The nanosheets of MoS_2 obtained by so-called micromechanical exfoliation method ([1]). In this method, one starts from a bulk crystal of the MoS_2 (Naturally occurred crystals of MoS_2 (SPi-SUPPLIES 429MS) was used in this work). And then peeling off the thick flake repeatedly using an adhesive tape. Thinner nanosheets can be obtained by repeating the peeling process. This process is shown in Fig.3.1(b). As the number of peelings increased (from 1 to 7), the area with the nanosheets becomes more transparent indicating the remaining nanosheets are thinner. We use the areas similar to number 7. The typical thickness of nanosheets obtained from such areas is < 100 nm. After preparing the ultra thin flake of MoS_2, they were transferred to Au films by pressing the tape against the surface of the Au substrate. Afterwards, the substrates were heated up to 110 ° C prior to the deposition in order to drive off the adsorbed water layer from the surface [32]. As a result, the increased yield of few-layer MoS_2 flakes achieved. A hot plate (ASONE-NINOS ND-1) utilized for this purpose.

3.2 Sample cleaning

After transferring MoS_2 nanosheets to the Au substrate, they were sonicated in acetone at 40C for 10 minutes using a sonicating bath (ASONE USD-1R). The sonication frequency was 40 kHz. This step is essential to remove most of the adhesive residues. Figure 3.2 (a) and (b) compares the surface before and after this procedure.

Most of the residues remove from the surface of the sample by the sonication procedure. However, some amount of contaminations with irregular shapes remain in the sample that only is observable by an AFM.

In order to remove the micrometer scaled adhesive residues from the sample surfaces, they were annealed using the resistively heating method in the e-beam-evaporator-vacuum chamber for 5 hours. The heating stage is a tungsten board with the dimension of 0.2 mm $\times$ 20 mm $\times$ 100 mm. The W board starts to glow at bias voltage of 0.6 V and current of 90 A. These conditions correspond to the temperature of 670° C measured by a radiation thermometer (CHINO-IR-AH).

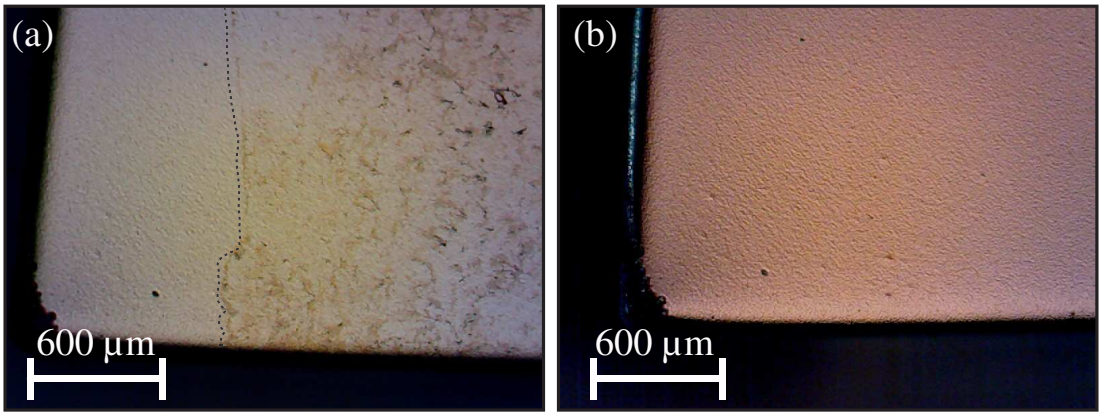

Figure 3.2: Optical microscope image of the substrate before (a) and after (b) sonication in hot acetone. The residue of adhesive tape dominant the right side of (a) marked by the dashed line. The magnification is 5x in both images.

3.3 Identifying MoS_2 nanosheets

In contrast to the most of the previous studies where MoS_2 or graphene devices were fabricated on Si/SiO_2 wafers [3, 1], it is not practical to make markers on Au substrates. The surface of Au is not sufficiently flat for the lithography procedure. As a result, to identify the nanosheets, several images with different magnification should be taken prior to AFM measurements. An optical microscope (Olympus BX51M) equipped with a camera (Moticam 2000) used for this purpose. The edges of the substrate, as well as large flakes, serve as guides to find the desired nanosheets under AFM camera (which has a constant magnification of 20×). Figure 3.3 shows a sequence of images used for inspecting the samples. Under magnification of 50× and 100, mes the nanosheets with the thickness of $<$ 5nm ($\sim$ 8 layers) are visible with a low contrast. After this step, the exact thickness of the nanosheets determined using the AFM.

3.4 Sample stages

As for STM and STS measurements, the glass slide matches best for our system as its linear-thermal-expansion coefficient is $\alpha = 8.5\ \mu m/K$. The typical com-

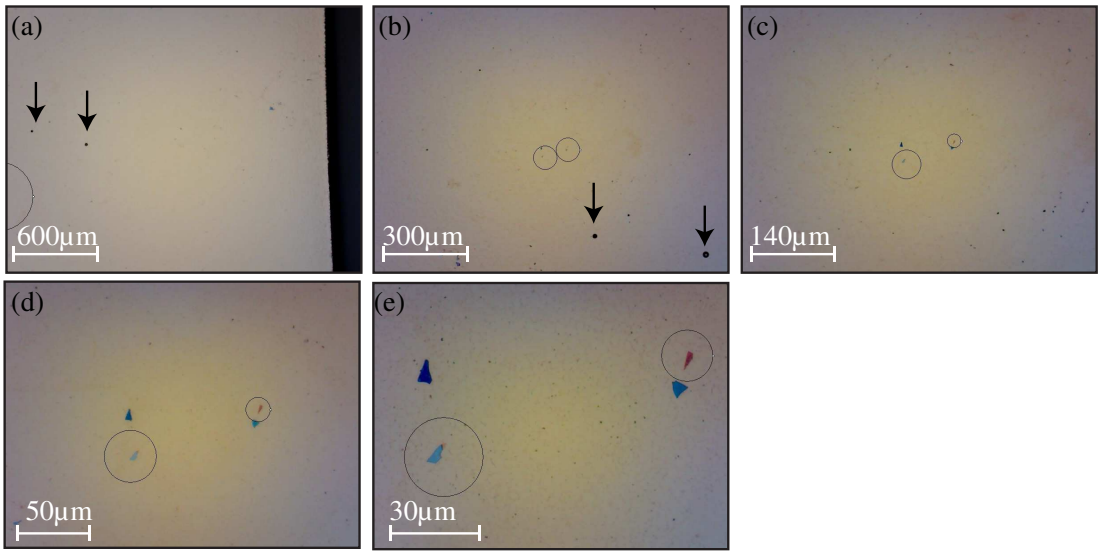

Figure 3.3: The sequence of optical microscope images used for navigating the AFM tip to the target flakes (marked by arrows and circles.) The magnification of 5×, 10×, 20×,50× and 100× in (a), (b), (c), (d) and (e) respectively.

mercial AFM stages made of anodized aluminium [see Fig.3.4 (a)] has $\alpha = 23.1$ $\mu m/K$ [33]. In the typical ambient AFM systems, the sample is mounted on the sample stage using adhesive materials such as grease, adhesive tape or silver paste. In the case of the grease and tape, the sample does not become perfectly rigid since the mentioned materials are not solid. Meaning that, they deform by time and this effect adds an extra unwanted drift source. However, sample mounting/unmounting process is easy in this case. In contrast, silver paste is more rigid but hampers the process of sample changing. Additionally, using the adhesive material might introduce contamination to the sample surface. To avoid all these issues, we designed and fabricated a sample stage that holds the sample by a spring [Fig3.4 (b)]. This stage has to main parts: stationary holder (part 1) and the mobile holder connected to a spring (part 2) (see Fig3.4 (b)). The sample gets fixed between these two parts. As for the part 1, we used a Si/Sio_2 wafer with the thickness of ~ 220 μm. A silver paint (Dotite) was used for fixing the wafer and dried at the temperature of 120 ° C. Such a thin part is required due to the vertical space limitation when the AFM head is mounted on the sample

stage. Therefore, such a sample stage prevents the usage adhesive materials, and it facilitates the procedure of mount and substitution of the samples. The detail of the design is brought to Appendix A.

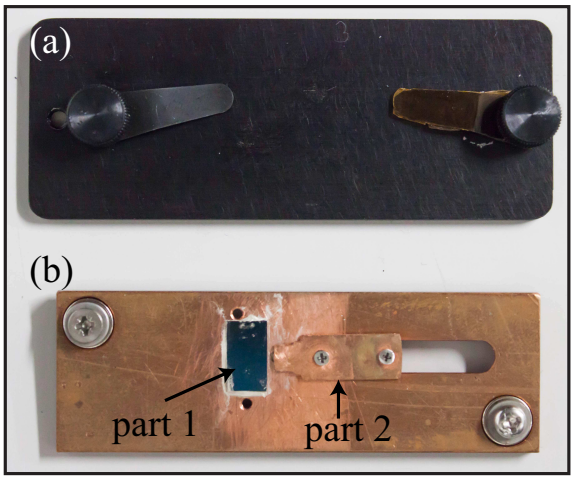

Figure 3.4: (a) The AFM anodized Al sample stage. (b) Home made sample stage

3.5 Surface analysis of gold substrates

In this section, the corrugations of Au substrates as well as MoS_2 nanosheets deposited on these samples are compared.

The typical AFM image of Au/glass is depicted in Fig.3.5 (a). The profile line taken across the straight dashed line reveals that the corrugation on this surface is relatively long range due to the formation of Au grains marked by curved dashed lines. The roughness of 11.13 nm measured by calculating the root mean square (RMS) of the topography. The average length of the grains, i.e. the wavelength of the corrugation, is $\sim$ 1.25 μm. Figure 3.5 (b) illustrates the area distribution of the grains. The peak is located at about 1.5 μm^2 which corresponds to the area of the 75 % of the grains.

As for Ti/Au samples, the AFM topographies reveal the roughness of RMS = 4.51 nm that is lower than that of Au/glass. The grains observed on Au/glass

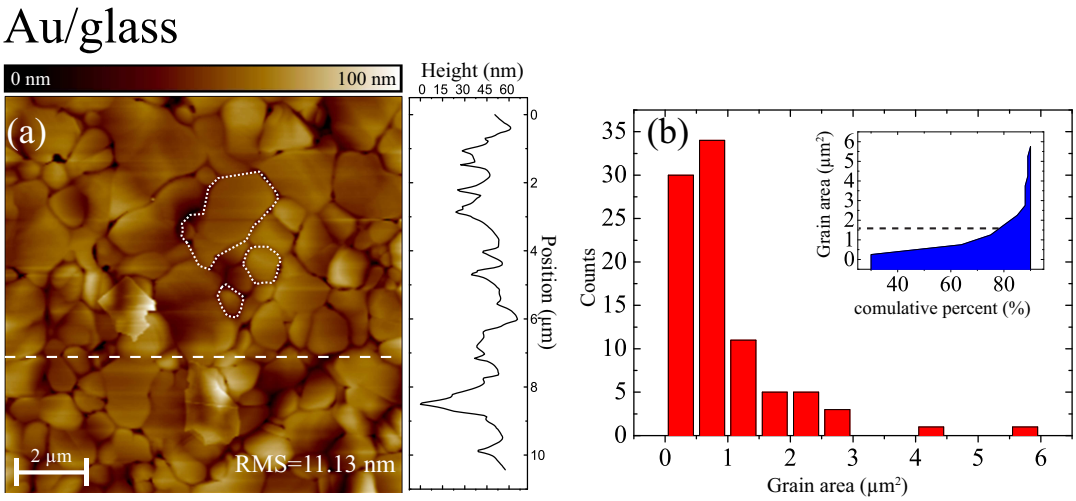

Figure 3.5: Characterization of Au/glass substrates: (a) The AFM topography of Au/glass surfaces with the roughness of RMS= 11.13 nm. The height profile taken across the dashed line is shown on the right side of the figure. (b) Histogram of the area of the grains in (a). The inset represents the cumulative distribution in %.

are not present. Instead, the surface exhibit bubble-like features [see Fig.3.6 (a)]. The profile line taken across the dashed line has a larger frequency compared with Au/glass indicating the smaller corrugation length of $\sim$ 100 nm. The objects with sharp edges are MoS_2 nanosheets. The zoomed AFM image of the flake marked by dashed square is shown in Fig.3.6 (b). This sample holds thin and thick areas with the average thickness of 2.88 nm ($\sim$ 4 layers) and 18.43 nm ($\sim$ 28 layers) respectively. Three gaussian-fitted peaks of a, b and c correspond to the thickness of the substrate, thin and the thick areas. Similar to MoS_2 nanosheets deposited on Au/glass, the substrate-induced corrugations are more pronounced on the thin flakes.

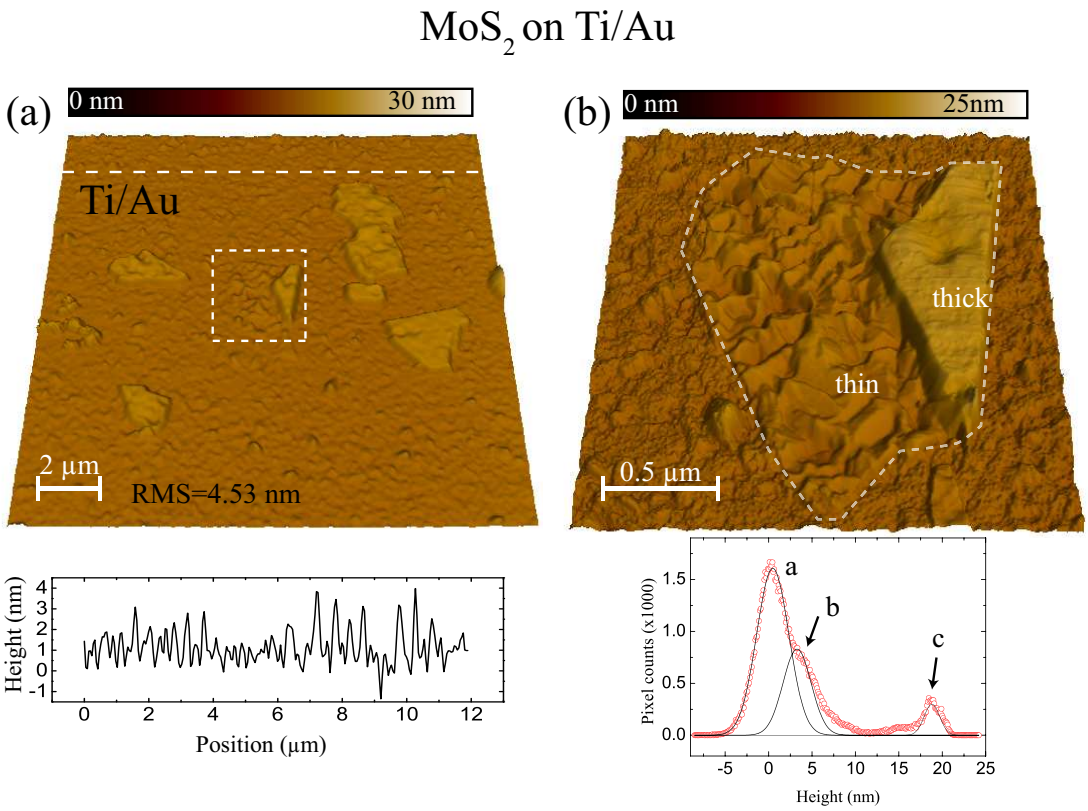

Figure 3.6: Characterization of Ti/Au substrate and MoS_2 nanosheets: (a) AFM image of Ti/Au surface. The height profile taken across the dashed line is shown in the lower part of the figure. (b) Zoomed AFM image of the MoS_2 flake denoted by dashed square in (a). A thin (2.88 nm) area with ripples and a relatively thick flat (18.43 nm) area within the MoS_2 flake are evident.

3.6 Characterization of the MoS_2 nanosheets deposited on Au/glass

3.6.1 MoS_2 roughness

The observed corrugations on MoS_2 nanosheets reflect the shape of the grains of underlying substrates. The effects of substrate on topography of thin ($\sim$ 20 nm), and thick ($\sim$ 50 nm) flakes are presented in Fig.3.7 (a) and (b). Specially, thin flakes are more prone to the topography of Au than thicker nanosheets that tend to be flatter. Figure 3.7 (c) shows the roughness of the nanosheets that are estimated from the full-width half maximum (FWHM) of the height of the regions (indicated by dashed squares). The FWHM for thinner and the thicker nanosheets [Fig. 3.7 (a), (b)] are 2.3 nm and 13.0 nm.

The thickness of the nanosheets can not be easily estimated from the profile lines since the surface is not flat. Therefore, we extract the thickness by subtracting the average height of the whole nanosheet from that of the Au substrate. As shown in the lower portion of Fig.3.7 (a), the histogram of the height distribution of the whole scanned area has two peaks. The left peak, which is offset to zero, corresponds to the height of the Au substrate and the right peak indicates the height of the nanosheet. Similar method is used for the thickness estimation of nanosheet shown in Fig. 3.7 (b).

3.6.2 lateral size and thickness Distribution of the MoS_2 nanosheets

In this section, the distribution of the average lateral size (l) and the average thickness (h) of the nanosheets deposited on Au/glass are discussed. Here, we analyzed 20 nanosheets. The thickness of the nanosheets is estimated using the method described in Sec. 3.5 and the lateral size is determined by measuring the average length of the nanosheets. The histogram of the lateral size is shown Fig. 3.8 (a). The minimum and the maximum l are 1.2 μm and 12.7 μm. Among the measured nanosheets, $l = 2.3$ μm is the most frequent lateral size. The histogram of the thickness is depicted in Fig. 3.8 (b). The minimum and the maximum h

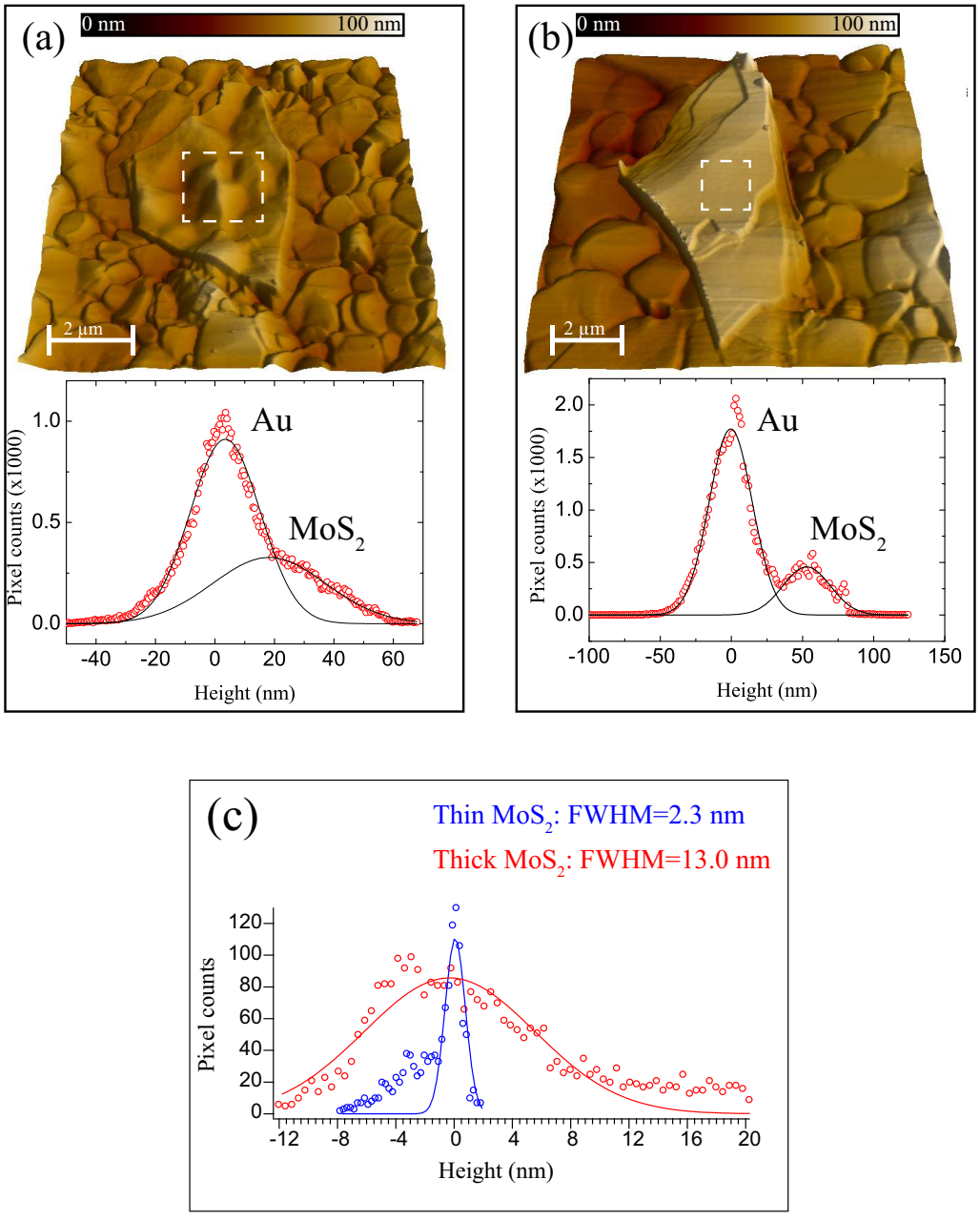

Figure 3.7: Characterization of MoS_2 nanosheets deposited on Au/glass substrates: (a) The AFM topography of a $\sim$ 20 nm thick MoS_2 flake whose surface highly affected by the corrugation of the underneath substrate. (b) An AFM image of a relatively thick and flat ($\sim$ 50 nm) nanosheet. The average thickness of the flake measured from the height distribution histograms shown in the lower portion of the figure.(c) The blue and the red curve shows the height distribution of the region marked in (a) and (b). The roughness is estimated from the FWHM of the fitted Gaussian curves.

are 0.9 nm and 51.1 nm. The thickness of the 12.0 nm and 21.0 nm are the most frequent.

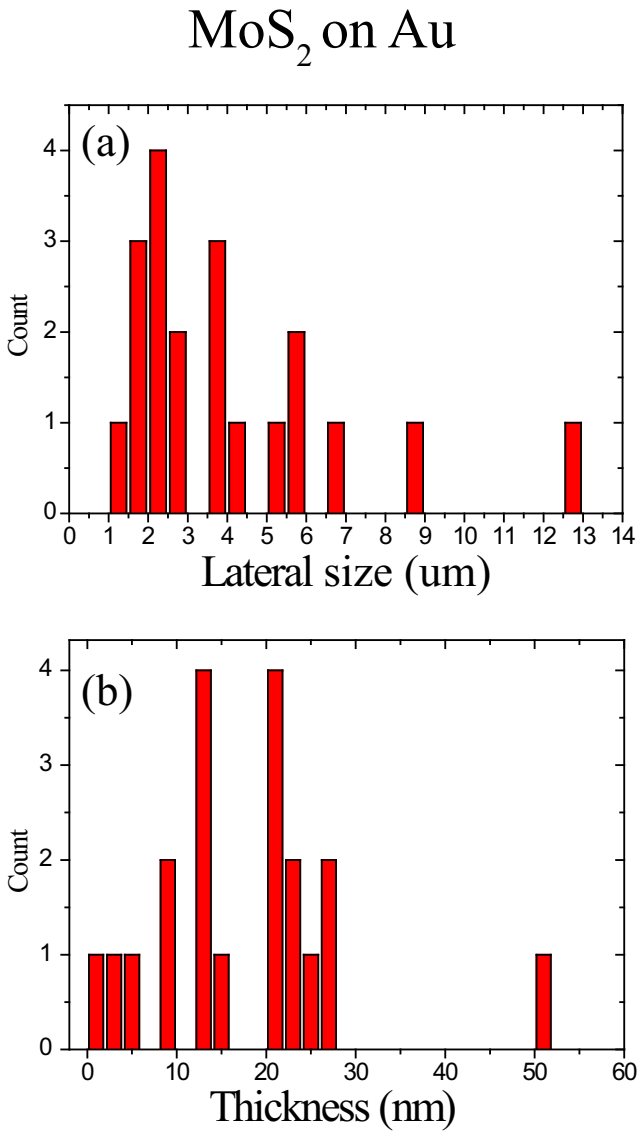

Figure 3.8: The distribution of the lateral size, (a) and the thickness,(b), of the MoS_2 nanosheets.

Chapter 4

Development of the AFM−assisted STS

4.1 Introduction

In this chapter, the development of an AFM−assisted STM is discussed. The motivation behind of the development of this system is to have a fast and accurate access to a desire area on wide samples such as MoS_2 flakes, which can have width of a few micrometer [2], by using an AFM and investigating electronic structure of that specific area by switching to STM function. The results shown in this chapter are partially published in [34].

AFM offers further advantages when used with STS measurements, especially at room temperature. Each LDOS spectroscopy is done by recording the differential conductivity $\mathrm{d}I_t/\mathrm{d}\,V_s$ with sweeping the sample voltage V_s, which determines the sample energy. Here, I_t is the tunneling current. During spectroscopy, STM feedback loop (FBL) is disabled to maintain a constant tipsample distance that otherwise would change with sweeping V_s [20]. Without the FBL, the vertical thermal drift (VTD) is not compensated for and therefore affects the intrinsic LDOS curve. This problem limits the total V_s sweeping time determined by the sweeping range, the number of the data acquisition and the averaging time for each acquisition, which, respectively, determine the energy range, energy resolution and signal-to-noise ratio (S/N) of the data. Using AFM FBL, one can

compensate for the thermal drift during spectroscopy and therefore increase the total V_s sweeping time. This enables us to perform room temperature (RT) measurements of LDOS over a wide energy range at a high energy resolution and high S/N.
In the following sections, using our AFM−assisted STS, we show alternating AFM and STM measurements using a metallic cantilever under ambient conditions. We demonstrate AFM-assisted rapid access to a selected area prior to STM measurements. Moreover, we present tunneling spectroscopy with activated AFM FBL that suppresses the effect of VTD on the I_t with the help of repulsive force due to a thin layer of insulating contamination formed on the tip and/or sample.

4.2 Measurement setup

Figure 4.1 shows a schematic model of our microscope. We used Asylum Research AFM (MFP-3D, CA, USA) with a standard chip holder. In order to utilize it for STM, we used a metallic Pt/Cr-coated cantilever , with the thickness of 25 and 5 nm repectively, and connected it to an external operational-amplifier current-to-voltage convertor (FEMTO-DLPCA-200, Berlin, Germany) with a gain of 10^9 V/A. An external lock-in amplifier (Signal Recovery 5210; AMETEK, TN, USA) was used for the STS measurement. The peak-to peak modulation voltage was 150 mV at the frequency of 83.3 Hz. To switch the z-FBL input between deflection (q) and the tunneling current signal (the upper right block in Fig. 4.1), we modified the source code of the software (Asylum Research-MFP3D12084).

The AFM images were taken in amplitude-modulation (AM) attractive mode, confirmed by a phase larger than 90° during imaging. To avoid a tip crash, we carefully chose a ratio of the free air (A_0) and set point (A_s) oscillation amplitudes A_s/A_0 (0.9) close to 1. An example of AM-AFM image of HOPG taken in net attractive force regime is depicted in Fig.4.2. Several cantilevers were tested for STM measurements. Cantilevers with spring constant of $K \sim 50$ N/m (Budget Sensors Tap300-G; TED PELLA, CA, USA) were found to be stable enough for STM measurement. The spring constant of the cantilevers used in this work were determined by the thermal noise method [35] after each experiment. A

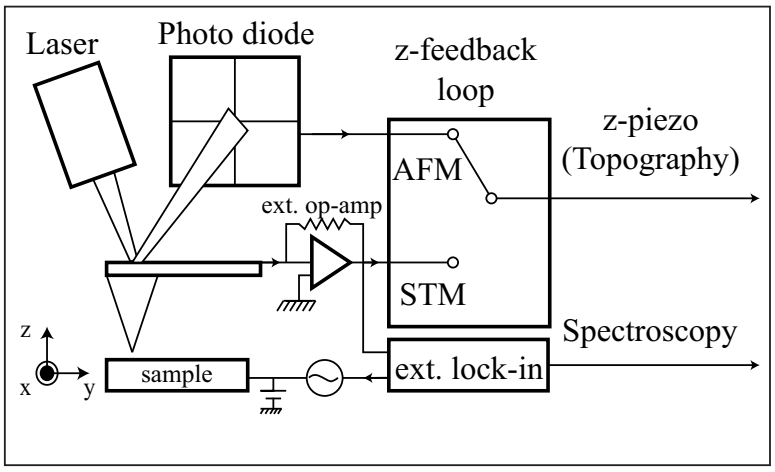

Figure 4.1: Schematic representation of AFM−assisted STM. External operational amplifier (ext. op amp) and lock-in amplifier added for detection of I_t and STS signal. In the case of AFM (STM), the z-feedback loop input is the deflection (tunneling current) signal.

lower-K cantilever caused a tip crash that occurred right after the tip started moving. This might be due to mechanical instability of the cantilever [35]. All the measurements were done on HOPG under ambient conditions.

4.3 Current and force regimes

Figure 4.3 shows typical I_t and force (F) curves as a function of z-piezo displacement (Z_p) measured simultaneously without feedback. The force between points 2 and 3 is in repulsive regime (positive q) with a gradient of $\Delta F/\Delta Z_p = -44$ N/m, which we utilized for the AFM-FBL during STS measurements. The I_t-Z_p curve shows an exponential behaviour (inset of Fig. 4.3), i.e. signature of the tunneling current.

The repulsive forces at which we performed STM and STS measurements indicate that the tip and the sample were mechanically coupled. The same tendency was also observed in STM measurements performed under ambient conditions [36, 37, 38, 39, 40] especially prior to electrical contact (i.e. in the tunneling current regime) [41]. This behavior interpreted as tunneling through an insulating layer

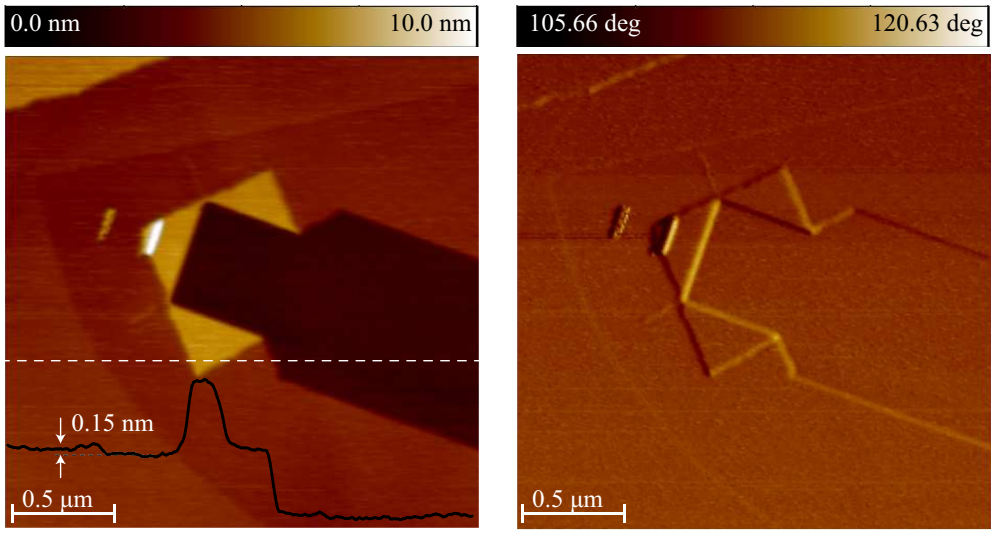

Figure 4.2: Example AFM image of HOPG taken in net attractive regime: (left) AFM topography of HOPG. The structure is formed randomly in the sample preparation procedure of cleavage. The height profile taken across the dashed line shows an atomic step of 0.15 nm. (right) The phase image measured simultaneously as the left figure. The average value greater than 90° is an indication of repulsive regime.

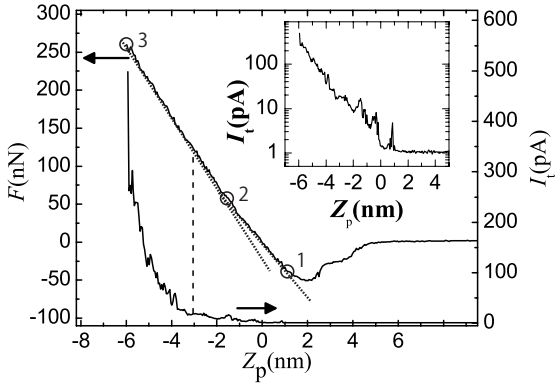

Figure 4.3: Simultaneous measurement of I_t and F as a function of Z_p. In this measurement, grounded tip approached to the biased sample ($V_s = 0.5$ V) until $I_t = 500$ pA was detected and then tip retracted. This procedure repeated on the same position and I_t and F averaged over three repeated measurements. The origin point of $Z_p = 0$ nm is arbitrary chosen to be at the point where I_t starts to flow. The inset shows log scale of I_t (Z_p) curve indicating exponential behavior of the current. The spring constant is 44.76 N/m

caused by unavoidable contamination on a tip and/or sample surface [42].

4.4 Alternative AFM/STM on HOPG

Figure 4.4 (a) shows an AFM image taken in the relatively large area of 10μm $\times$ 10μm, which includes a maximum surface corrugation of 11 nm (bright strand passing from upper to lower). This image was recorded at the scanning speed of 15 μm/s for a total time of 5.6 min.

If STM was used to scan the same area, the scanning speed (total scanning time) should have been reduced (increased) at least three orders of magnitude to not get a tip crash. After scanning the large area, we selected a smaller area of 0.5μm $\times$ 0.5μm [square in Fig.4.4 (a)] and performed AFM and STM imaging [Fig.4.4 (b), (c)]. As it shown, steps on the HOPG surface is smeared out in AFM topography whereas in STM image a sharp step can be seen. This is due to different lateral resolution of AFM and STM. Although the tip was same for both cases but lateral resolution of tip in case of STM is higher since the tunneling current drops exponentially by tip-sample distance and therefore the effective area of the tunneling is small than that of the force sensing.

4.5 Compensation for vertical thermal drift

Next, we examined the VTD, which may affect the standard spectroscopy measurement performed with disabling FBL. Figure 4.5 shows time dependence of z-piezo displacement measured by a sensor (linear variable differential transformer (LVDT) sensor, which accurately measures the z-piezo displacement [43]) with enabling AFM in contact mode. In this mode, the tip is in contact with the sample and the feedback keeps the deflection (bending) of the cantilever constant. Therefore, the displacement of the z-piezo reflects the movement, i.e. thermal drift, of both the AFM head (which includes the cantilever and z-piezo) and sample stage. The positive slope of the graph indicates that the FBL retracted the tip from the sample surface as a result of FBL compensation for the reduced tipsample distance (Z_g) due to the thermal drift. The drift rate estimated was

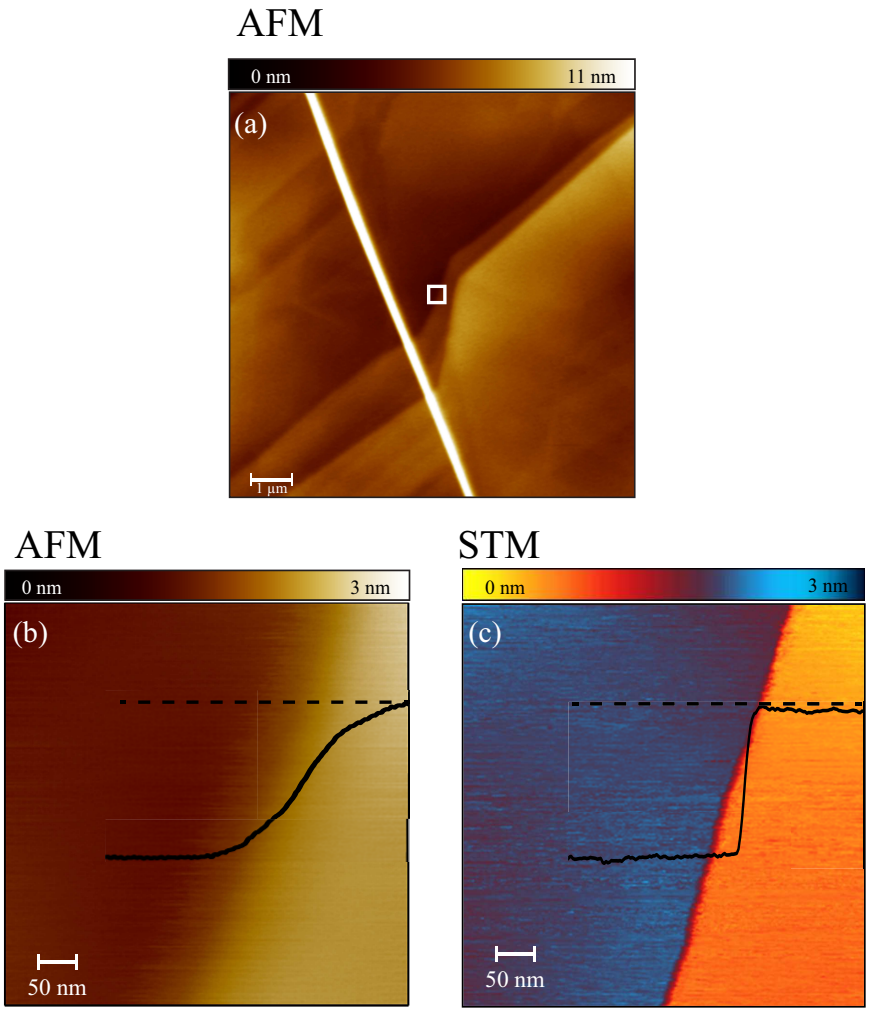

Figure 4.4: Alternating AFM and STM imaging on selected area of an HOPG. (a) Fast and large area scanning by AFM. (b) AFM image of the marked area in (a).(c) STM image of the selected area marked by the white square in the center of (a). The solid line is the profile along the same line as the dashed line. The cantilever spring constant is $K = 52$ N/m. Sample voltage and tunneling current set point are $V_s = 1.0$ V and $I_s = 50$ pA.

$\nu = 1.1$ Å/s. Note that, this result is an example of the vertical thermal drift and it varies time to time due to the thermal fluctuation. The estimated drift rate implies that the time required for a single spectroscopy is limited to below 1 s. Otherwise, the thermal drift can cause a substantial artifact in the measured LDOS curve and even a tip crash. This limitation is not a problem at low temperature, because the thermal drift is negligible. However, at RT, as we showed, a much larger VTD limits the measurement time and hence limits the energy range, the energy resolution, and the S/N of the LDOS data.

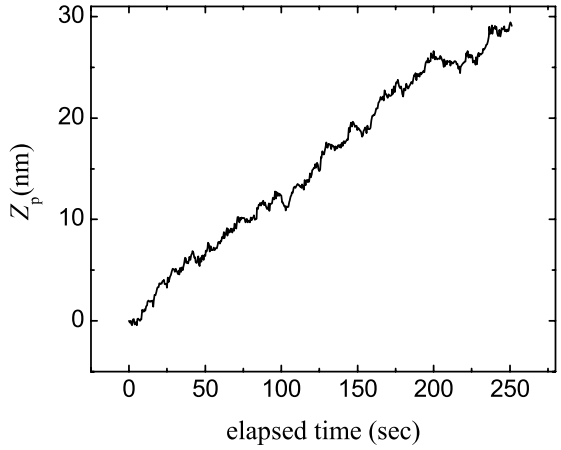

Figure 4.5: Measurement of VTD. This measurement was done in contact AFM mode using a cantilever with $K = 3.7$ N/m. The VTD rate of $\nu = 1.1$ Å/s was estimated by fitting a line to the graph.

As mentioned in sec. 2.6.2, one of the challenges in scanning probe techniques is the effect of thermal drift (TD) on the imaging and spectroscopy. The TD rate in low-temperature systems is very low at the order of few the tens of pm/h. Therefore, in these system, the TD is not an issue. However, in room temperature, the effect of TD become more pronounced. The drift rate can reach few nm/h that is two orders of magnitudes more than that of the low-temperature systems. The lateral X and Y drifts appear when the scanning speed is at the same order as the drift rate. Also, it arises in spectroscopy measurements where the tip stops at each grid points and therefore the required acquisition time is longer than typical scanning. As a result, the topography image of AFM and STM in both cases of

low-speed scanning or spectroscopy elongates in the drift directions. The effect of vertical thermal drift, i.e. in the Z direction, is more crucial in the spectroscopy measurements. Since, in contrast to scanning mode, no feedback is activated and therefore the tip-sample gap, Z_g, changes by the thermal drift. Especially in lock-in technique measurements, the time, that the feedback is deactivated, can reach 10 seconds. One solution to this issue at room temperature is proposed by Abe *etal*. [11]. In this method, first the drift rates in all X, Y, and Z directions are measured. Second the scanners are derived in the opposite direction to that movement caused by of the drift at the same rate, i.e. velocity. In this solution, it is assumed that the drift rates are constant over the time between the first and the second steps, and therefore it is a so-called passive TD compensation. Although, the assumption of the constant drift rates can be valid within few minutes, it cannot be extended for the time span of few hours since the temperature does fluctuate and affect the TD rates. Therefore, in the mentioned method, one needs to measure the drift rates before each experiment. In this thesis, we proposed an active vertical TD compensation for STS measurements where a static (DC) AFM feedback is used to keep the Z_g constant during the tunneling spectroscopy. This method is a so-called active TD compensation since the tip-sample distance is actively controlled depending on the interacting forces between the tip and the sample. Therefore, the TD rate does not need to be estimated before each STS measurement.

Figure 4.6 represents I_t and q signals as a function of time during which the STM-FBL deactivated and switched into AFM. Both signals increase dramatically when the FBL is cut. This is due to decrease of Z_g as a consequence of thermal drift. In contrast, when the AFM-FBL is activated, I_t maintains constant indicating the stable Z_g.

Figure 4.7 (a) and (b) illustrate the simultaneous measurement of q and I_t respectively, as a function of time. In the region I of the Fig. 4.7 (a) and (b) (left portion of the plots), STM feedback is activated. In the region II, the feedback is switched into AFM FBL. We found that changing the FBL does not change the deflection, and hence the tunneling current remains the same. Moreover, after switching the FBL, the tunneling current was maintained for >70 s, indicating that AFM FBL compensated for the VTD. The noise of q (q_{Sdev}) and I_t (I_{Sdev})

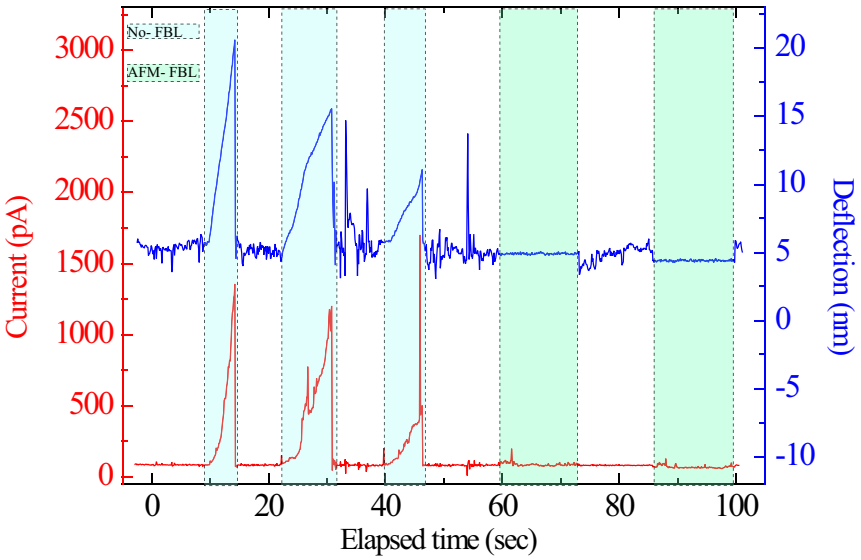

Figure 4.6: Current and deflection vs. time. The FBL is deactivated and set to AFM in light blue and green areas respectively. In non-marked areas tip is stabilized with STM-AFM at $V_s = 1.0$ V and $I_s = 50$ pA.

are determined by estimating the standard deviation of these signals. The q_{Sdev}, is 27.5 and 12.6 pm in the region I and II respectively while I_{Sdev}, is 5.2 and 4.9 pA in the region I and II respectively. The larger q_{Sdev} in a region I compared to that in region II, indicates that FBL parameters, i.e. the proportional and integral coefficients, are not optimized enough to keep deflection constant as well as current.

4.6 AFM-assisted STS measurement on HOPG

The AFM-assisted tunneling spectroscopy was performed as follows. First, the tip was stabilized at a fixed Z_p in STM mode. Second, the deflection signal was acquired to determine the deflection value at the corresponding Z_p. Finally, before starting tunneling spectroscopy, STM FBL was switched to AFM FBL, which used the determined deflection value as the FBL reference to keep the Z_g constant.

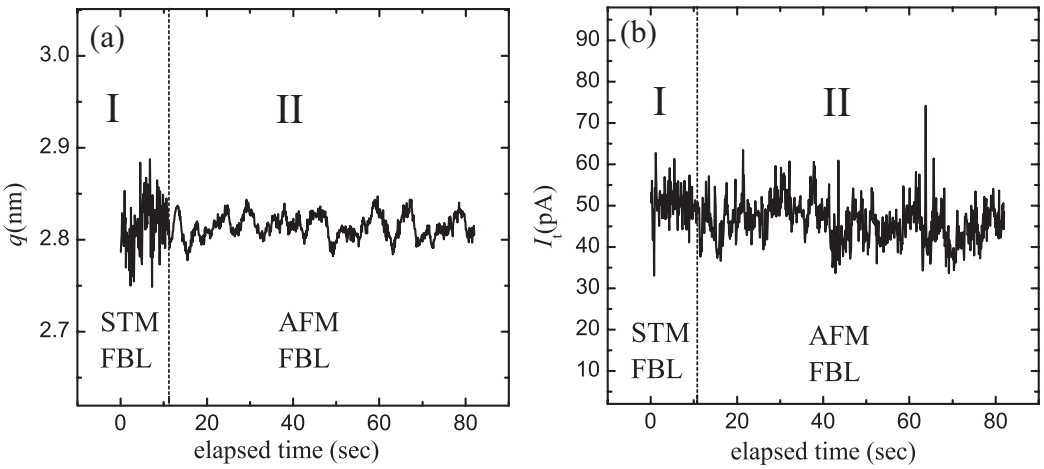

Figure 4.7: Switching STM FBL into AFM FBL to compensate for VTD. The stability of q and I_t before and after FBL switching indicates stable Z_p while compensating for thermal drift. The set point of tunneling current and sample bias are $I_s = 50$ pA and $V_s = 0.5$ V. The spring constant is $K = 52$ N/m for (a)and (b).

Finally, we conducted AFM-assisted single tunneling spectroscopy at $Z_p = 3.1$ nm and $I_t = 20$ pA (marked by the vertical dashed line in Fig. 4.3), using a lock-in amplifier at a total V_s sweeping time T = 30.1 s determined by the number of the data acquisition, n = 101, and the averaging time for each acquisition, = 300 ms. The obtained dI_t/dV_scurve (Fig.4.8) shows the typical V-shaped characteristic of HOPG in agreement with a previous result [44]. Moreover, the observed smooth curve implies a fairly high S/N and no tip crash in the long spectroscopy time. This indicates that AFM-assisted tunneling spectroscopy enables us to perform spectroscopy while flexibly tuning the energy range, energy resolution and S/N.

4.7 Effect of electrostatic forces on STS

It is known that the applied V_s induces the electrostatic force. Sweeping the V_s indeed varies the deflection (Δq) [Fig.4.9 (a)], which has a minimum near $V_s = 0.1$ V due to a mismatch of tip and surface potential [45]. Within the range used for

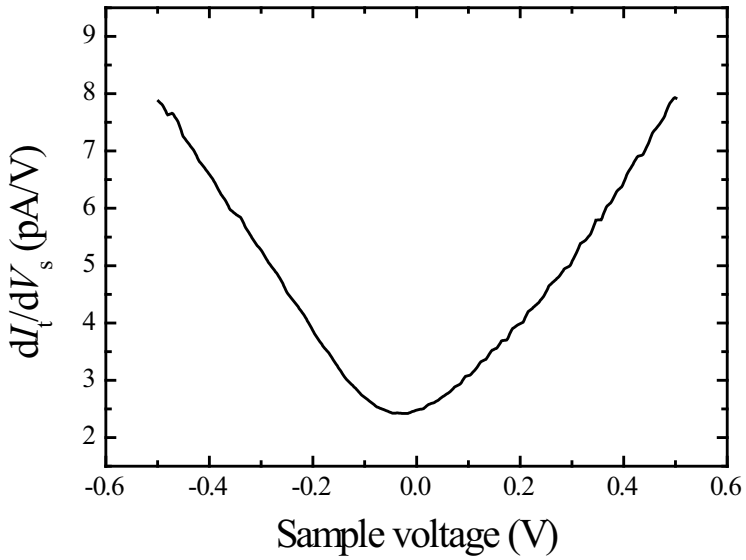

Figure 4.8: STS on HOPG. The curve shows the long measurement of $\mathrm{d}I_t/\mathrm{d}\,V_s$. The total measurement time was 30.1 s. The AFM FBL was activated during spectroscopy to compensate for the VTD. High S/N of $\mathrm{d}I_t/\mathrm{d}\,V_s$ signal indicates a stable Z_g. The set point of I_t and V_s are $I_s = 20$ pA and $V_s = 0.5$ V. The spring constant is $K = 44.76$ N/m.

the tunneling spectroscopy $-0.5V < V_s < 0.5V$, the maximum Δq is found to be 16 pm. To estimate the change in the tipsample gap (ΔZ_g), we used a previously proposed model [46]. According to this model, $\Delta Z_g = \Delta\ Z_p - \Delta\ q - \Delta Z_s$ [see Fig.4.9(b)]. Here, ΔZ_s is the deformation of the sample which is negligible because the sample is relatively rigid [46] compared with the cantilever and the gap (insulating layer) in our system. By roughly estimating the force gradient of $\sim$29 N/m between points 1 and 2 (Fig. 4.3), where ΔZ_g is nonzero, and dividing it by cantilever force constant ($K = 44.76$ N/m), we obtain $\Delta q = 0.65\ \Delta Z_p$. Substitution of the latter in the first equation yields $\Delta Z_g = 0.54\ \Delta q$. Therefore, a change in tip-sample gap $\Delta Z_g \approx 8.6$ pm may cause current change of $\mathrm{I}_t \approx 0.4$ pA. This value is only 2 percent of the tunneling current set point $Z_s = 20$ pA, implying that the effect of electrostatic force on $\mathrm{d}\mathrm{I}_t/\mathrm{d}\,V_s$ curves is negligibly small.

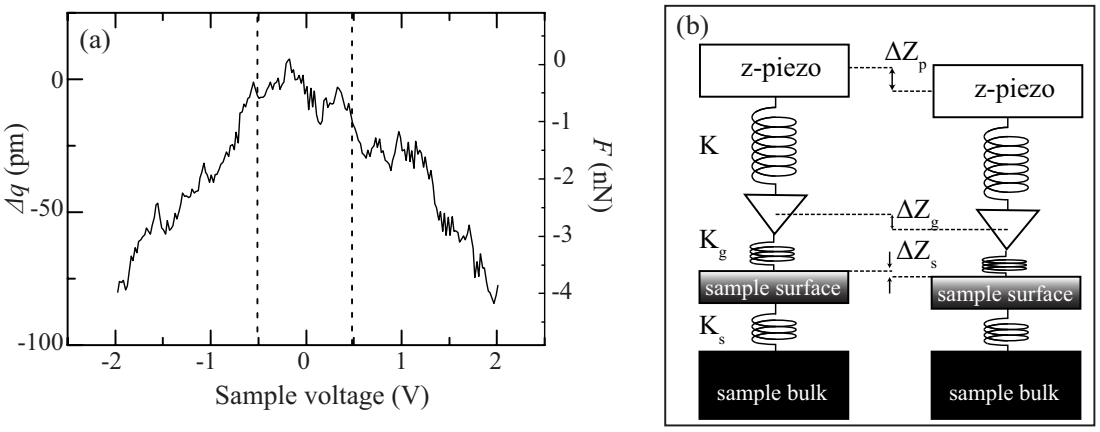

Figure 4.9: (a) Bias voltage dependence of the deflection. The resulting maximum change in tunneling gap is $\approx 8.6 pmat\, V_s = 0.5$ V, which leads to 2 percent change of I_t. Tip approach speed is 5 nm/s and the current trigger point is 20 pA. The tip retracted for 5 nm before voltage sweep to avoid tip crash. (b) Schematic of the mechanical model of the coupled tip and surface.

Chapter 5

Tunneling Spectroscopy on MoS_2 Nanosheets

In this chapter the AFM-assisted STM is employed to observe the local density of states of MoS_2 nanosheets deposited on Au (111) substrates.

5.1 Required condition for spectroscopy

To observe intrinsic characteristics of the MoS_2 nanosheets, we carefully chose the conditions for tunneling spectroscopy. The optimization ways are explained using data obtained on MoS_2.

The tip-induced band bending, which has been reported in STS measurements on the III−V semiconductors [47, 48], is an effect arises from the electric field of the tip. Band bending becomes more pronounced at high tunneling current setpoints (I_s) where the tip−sample distance diminishes. This effect appears in STS data as a shift or change in the bandgap of the semiconductor. Figures 5.1 (a) and (b) show the evolution of the I/V and dI/dV curves with increasing the I_s. The decrease of bandgap at higher setpoints is evident. In particular, the decrease of 0.14 eV in bandgap observed at I_s= 100 pA. This value is estimated from the the intercepts of the linear-fits to the band-edges. In this work, the extremely low current setpoints of 5 pA $< I_s <$ 20 pA were chosen to avoid tip-induced band bending.

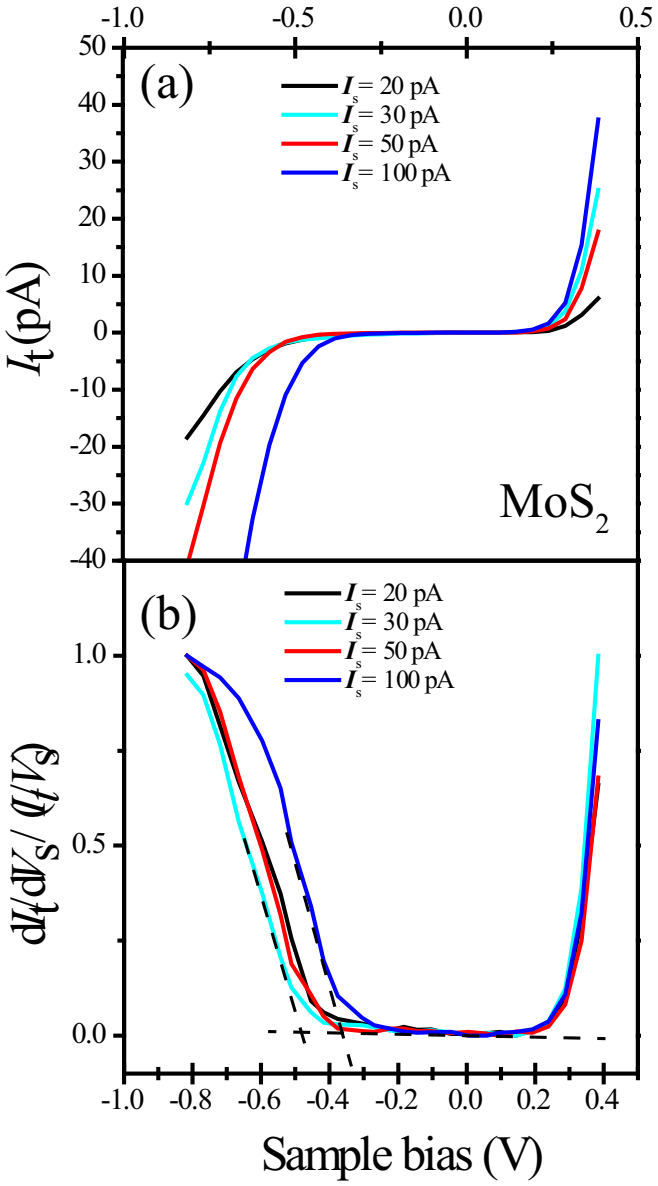

Figure 5.1: The tunneling current (a) and LDOS (b) versus sample bias at current setpoints of 20, 30 , 50 and 100 pA. The bias voltage is -0.80 V for all curves.

Another effect of high current setpoint is the collapse of the apparent tunneling barrier height (ϕ). Previous works have reported [46, 49] that ϕ decreases as a function of tip-sample distances.

By making the tip contact to the sample surface, tunneling junction breaks. Figure 5.2 shows the current as the function of z−piezo height (Z_p). The vertical axis is in log scale. The current is zero at $Z_p > 0$ nm. It increases linearly in the range of -13.2 nm $< Z_p < 0$ nm which is indicated by the blue line. The linear dependence of current on z−piezo height is an indication of the tunneling regime. For $Z_p < -21$ nm, the current saturates at 70 pA [red line in Fig. 5.2] in spite of further tip approach indicating that the barrier height collapses. For this reason, it is necessary to choose the current setpoints in the tunneling regime (less than $\sim$ 70 pA).

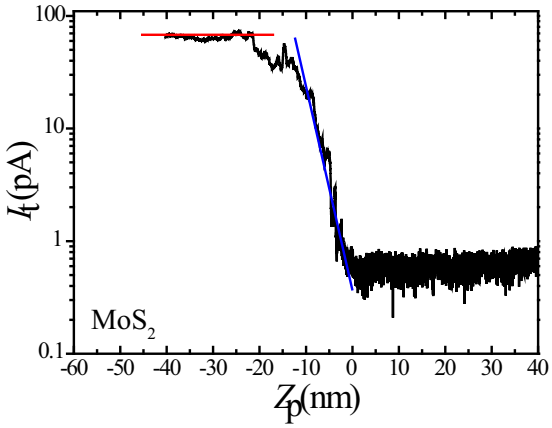

Figure 5.2: Current as a function of z-piezo height taken on MoS_2 nanosheet. The tunnel barrier height goes to zero for $I_t > 70$ pA. The tip approached at the speed of 5 nm/s. The spring constant of the cantilever is 38.32 N/m.

The tunneling current, I_t, as a function of tip-sample distance, z, can be written as follows [50]:

$$I_t \propto e^{2\kappa z}, \tag{5.1}$$

where

$$\kappa = \frac{\sqrt{2m\phi}}{\hbar}, \tag{5.2}$$

is the decay constant. The free electron mass and the reduces Planck constant are shown as m and $\hbar$ respectively. The apparent barrier height can be obtained from Eq. 5.1 and 5.2 as follows:

$$\phi = \frac{\hbar^2}{8m}\left(\frac{d\ln I_t}{dz}\right)^2 \approx 0.95\left(\frac{d\ln I_t}{dz}\right)^2 \tag{5.3}$$

Using Eq. 5.3 the apparent barrier height of 192 meV is extracted by linear fitting to the $I-Z$ curve. This value is lower the average of the work functions of Pt tip and MoS_2 , i.e. $(5.9+4.0)/2 = 4.7$ eV [4]. Taking into account the elastic tip−sample deformation in STS measurements on layered materials [46], the low barrier height is reasonable.

5.2 Point tunneling spectroscopy on MoS_2 nanosheets

Figure 5.3 (a) shows the AFM image of a MoS_2 nanosheet. Average thickness is estimated from the height histogram [lower row in Fig.5.3 (a)]. There are double peaks (open circle) which can be identified as two Gaussian peaks (solid curves). The peak means at $h_{Au} = -3.1$ nm and $h_{MoS_2} = 5.1$ nm correspond to the average height of Au substrate and MoS_2 respectively. As a result, the thickness of the MoS_2 nanosheets are $h_{MoS_2} - h_{Au} = 8.2$ nm that corresponds to 12 layers. The density of the states of the probe tip was examined prior to scanning tunneling spectroscopy on nanosheets. This was done by measuring the $I-V$ characteristic of Au substrate in the vicinity of the nanosheet. Observed $I-V$ curves [Fig.5.3 (b)] show typical ohmic behavior in the sample bias range of $\pm$. This indicates that the tip apex has a constant DOS. The same procedure was done for other STS measurements as well. In the cases, that the typical $I-V$ curve on Au was not detected, tips were treated by applying pulses to the bias voltage with the absolute magnitude less than 4V or replaced with a new tip. The tip then was retracted and moved to a lateral position on nanosheet, marked

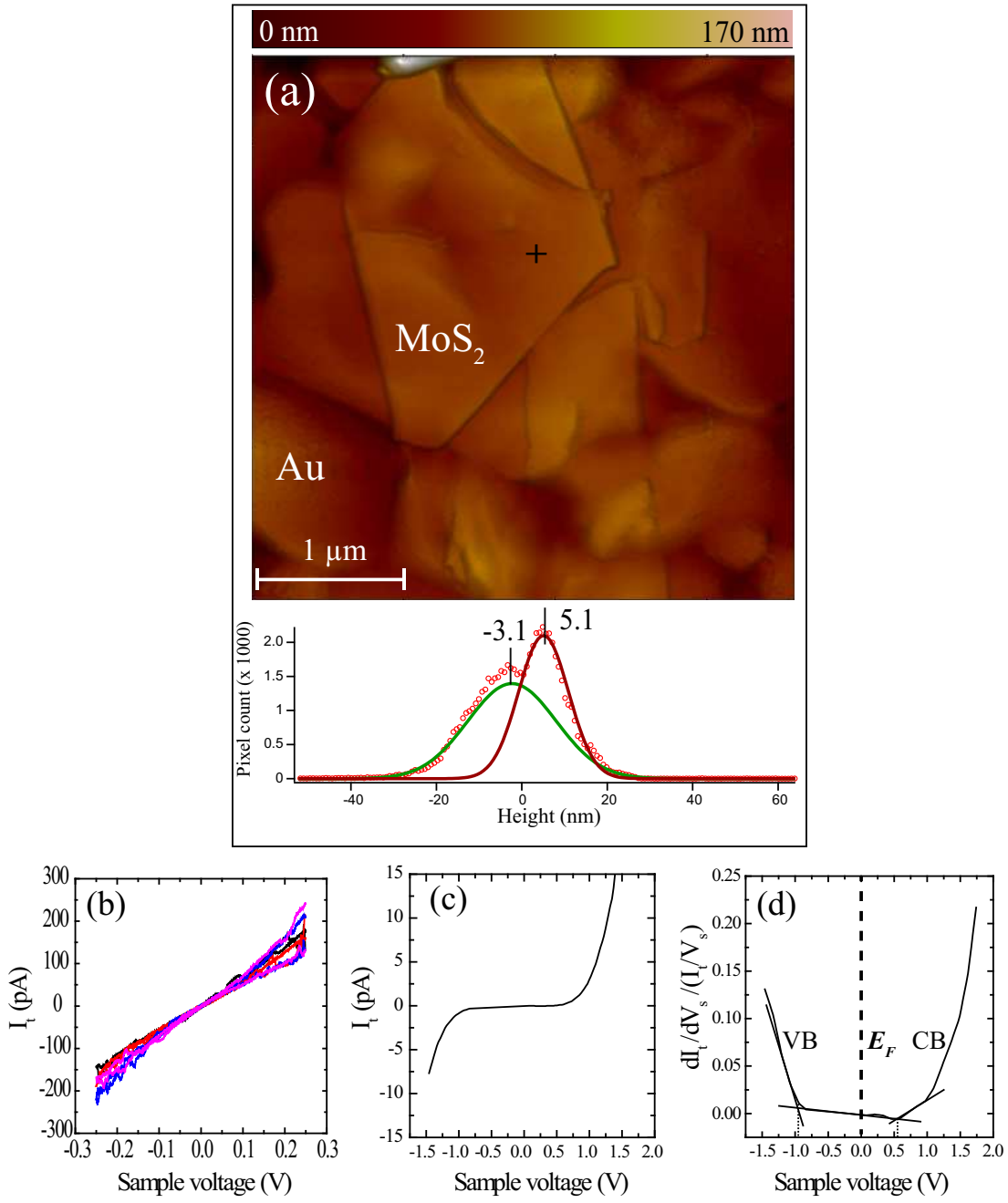

Figure 5.3: (a) Upper part: AFM topography image of a 8.11 nm thick MoS_2 nanosheet. Lower part: Height histogram. (b) $I-V$ characteristic measured on Au nearby the nanosheet in (a). I/V (c) and dI/dV (d) characteristics measured on the MoS_2 nanosheet shown in (a).

with a plus sign in Fig.5.3 (a). Afterward, the AFM-assisted STS measurements were performed in a similar way explained in chapter 4. The local conductance (I_t/V_s) and the normalized LDOS [d$I_t/dV_s/(I_t/V_s)$ (dI_t/dV_s)] versus sample bias (V_s) are presented in Fig.5.3 (c) and (d), respectively. These curves are average of 8 points STS measurements done in the same lateral position. Sample bias corresponds to the energy relative to the Fermi level. The Fermi level (E_F) is indicated by a dashed line at zero sample bias. The onset of VB and CB are located at - 0.91 and 0.60 eV respectively. Next section describes a method by which the onsets are estimated.

5.3 Determination of the band onsets and doping type

The energy onset of valance and conduction bands are determined by assuming linear onsets in normalized conductance [48]. Figure 5.4 (a) represents the point spectroscopy performed on a 3.6 nm thick nanosheet. As it is shown in the figure, the onsets are given by the intersections of the linear fits. The onset of VB and CB are located at - 0.51 and 0.42 eV respectively. The bandgap of 0.93 eV is determined by subtracting E_V from E_C. Another example of point spectroscopy taken from a 36.4 nm thick nanosheet is depicted in Fig. 5.4 (b). The E_V, E_C, and the bandgap are -0.32, 0.77, and 1.09 eV respectively. A quantity of E_V+ E_C is defined by which the doping type of the nanosheets is determined. If the summation of the VB and CB onsets is a positive value, the Fermi-level is located closer to VB than CB indicating the p-type behavior. Also, the negative value indicates that the Fermi-level is located closer to the CB than VB meaning that the conduction is n-type.

5.4 Precision of the STS measurements

The reproducibility of the STS measurements was examined by repeating the STS on the same lateral point using the same tip. To estimate the precision by which spectral positions are measured, the variation of the VB and CB was

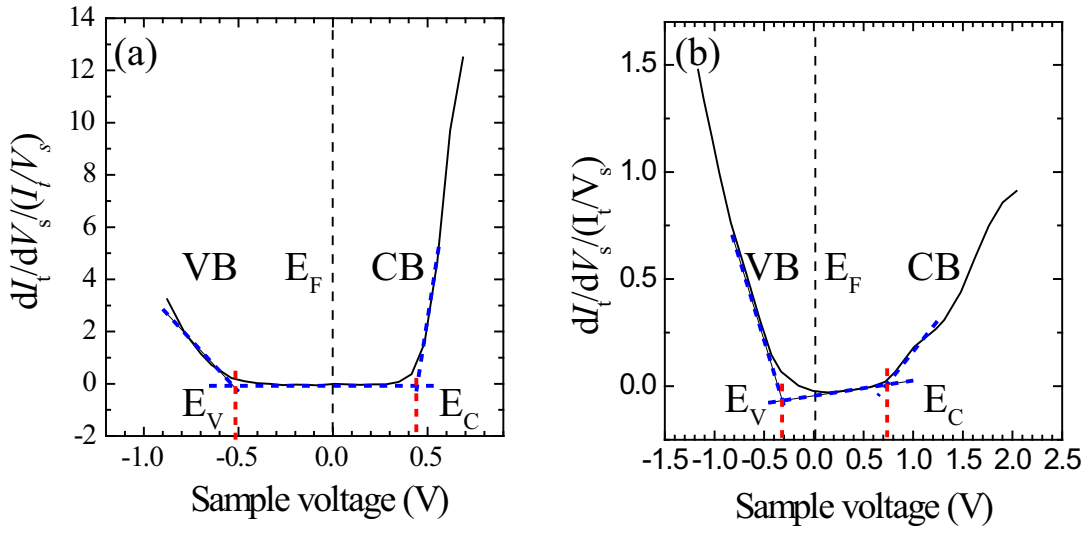

Figure 5.4: Determination of the band onsets and the doping type. (a) A 3.6 nm thick nanosheet shows n-type behavior. (b) P-type of doping is observed for a 36.4 nm thick nanosheet.

measured. As shown in Fig. 5.5 the band onsets were determined by the previously mentioned method in Sec. 5.3. The valance band varies in the range of $E_{Vmin}-$ = -0.46 eV and E_{Vmax} = -0.42 eV. The variation of the valance band is determined to be $\Delta E_V = E_{Vmax} - E_{Vmin}$ = 0.04 eV. The CB change is in the range of $E_{Cmin}-$ = 1.00 eV and E_{Cmax} = 1.05 eV. The variation of the valance band is determined to be ΔE_C = 0.05 eV. Choosing the higher band-onset shift, we defined the precision of ± 0.05 for the point spectroscopy.

In addition, the reproducibility of the tunneling spectra was considered for the cases when different tips were used. Figure 5.6 (a) illustrates the measurement performed with two differents tips on the same lateral point on sample A. The tip are named tip 1 and tip 2. Estimated VB onsets of the spectra taken by tip 1 are E_V^{tip1} = -0.63 eV and E_V^{tip2} = -0.50 eV respectively. The difference of these two values is ΔE_V = 0.13 eV. The CB onsets are E_C^{tip1} = 0.25 eV and E_C^{tip2} = 0.28 eV. The difference of these two CB onsets is ΔE_V = 0.03 eV. Same procedure was performed on another nanosheet designated as sample B [Fig.5.6 (b)]. The VB onsets are E_V^{tip1} = -0.45 eV and E_V^{tip2} = -0.33 eV which gives the difference of

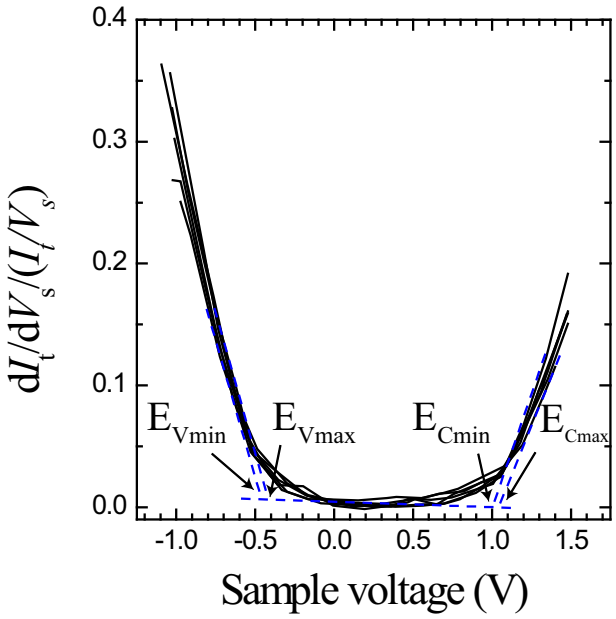

Figure 5.5: Reproducibility of the tunneling spectra using the same tip in the same lateral position. The precision of ± 0.05 is defined.

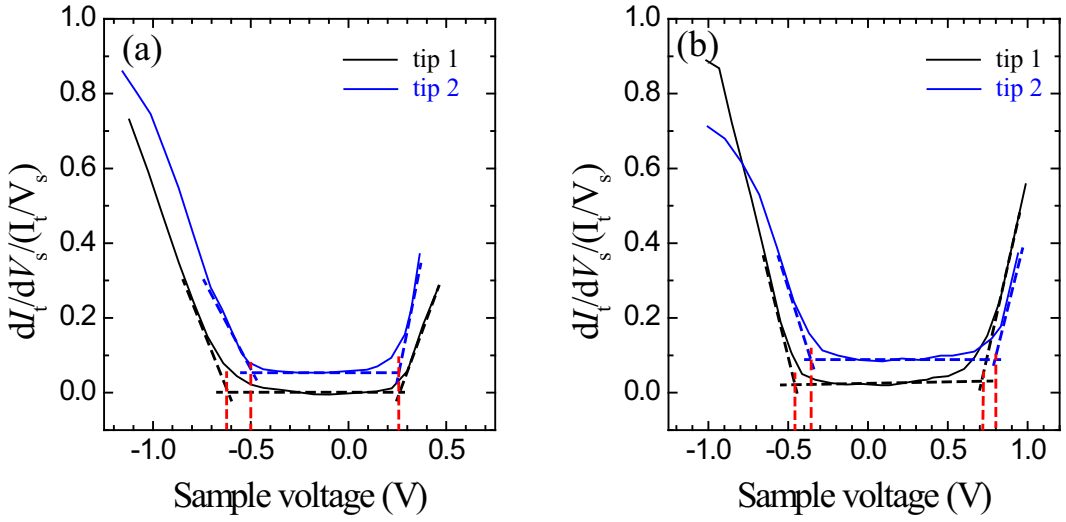

Figure 5.6: Presicion of STS taking into account the different tips. The variation of ± 0.13 eV is considered as the tip effect in the spectroscopy.

Sample No. (code)	Thickness (nm)	E_V ($\pm 0.13eV$)	E_C ($\pm 0.13eV$)	$E_C + E_V$ ($\pm 0.18eV$)	dope type	Bandap ($\pm 0.18eV$)
1 (7-2-1)	3.6	-0.51	0.42	-0.09	n	0.93
2 (6-1-6)	8.2	-0.91	0.56	-0.35	n	1.47
3 (6-1-3)	13.6	-0.20	1.03	0.83	p	1.25
4 (7-1-4)	13.8	-0.63	0.25	-0.38	n	0.88
5 (5-2-1)	20.7	-0.24	0.51	0.27	p	0.75
6 (4-1)	22.9	-0.50	0.85	0.35	p	1.35
7 (7-2-4)	26.1	-0.45	0.71	0.26	p	1.16
8 (6-1-7)	36.4	-0.32	0.77	0.45	p	1.09

Table 5.1: Summary of the point spectroscopy results

$\Delta E_V = 0.12$ eV. The CB onsets located at $E_C^{tip1} = 0.71$ eV and $E_C^{tip2} = 0.79$ eV that reults in $\Delta E_V = 0.08$ eV. From these measurements and taking into account the highest shift in the onsets, the precision of $\pm$ 0.13 eV is defined as the effect of the diffent tip in the spectroscopy. The shift in the spectra taken by different tips can be attributed to the change of the tip DOS due to for example recombination of the tip apex [51].

The LDOS measurements were done on several nanosheets. The summary of the estimated quantities of the thickness, E_V, E_C, doping type, and the bandgap are given in Table 5.1. Figure 5.7 shows the thickness dependency of the doping type of the nanosheets. The thicker nanosheets, i.e. thicker than 14 nm, have a tendency to show p-type behavior. The n$-$ type conductance is typical in the transport measurement performed on MoS_2-based devices [3, 12, 4, 13]. However, ambipolar behavior has recently been reported in thick nanosheets ($>$ 40 nm) where the substrate effects, i.e. short-ranged disorders caused by roughness or chemical bonding) was excluded using polymethyl methacrylate (PMMA) [52]. These results suggest that the substrate can affect the doping type of the nanosheets specially the thin ones.

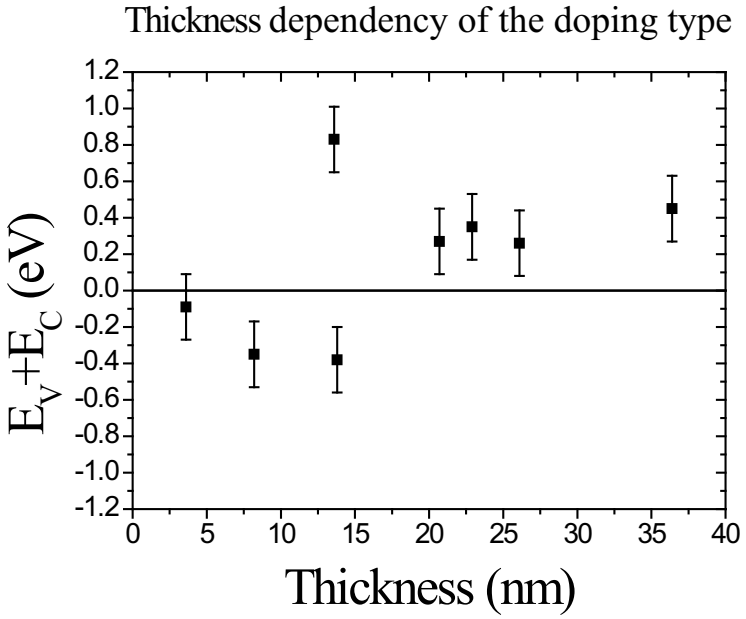

Figure 5.7: Thickness dependency of the doping type. Nanosheets thicker than $\sim$ 14 nm show p-type behavior.

5.5 Spatial mapping of LDOS on MoS_2 nanosheets

To investigate the spatial dependency of the electronics properties of nanosheets, particularly doping behavior, I developed the AFM software codes in order to perform line (or 1D) and two dimensional (2D) tunneling spectroscopy. The coding detail is brought in Appendix B. The procedure is very similar to standard spatial mapping of LDOS in constant current mode, where the tip-sample separation is controlled by tunneling current. The only difference is that the AFM feedback loop is activated during the STS measurements. To minimize drift effect of X and Y scanners, the I/V curves measured by fast sweeping of the sample voltage (500 ms) and the corresponding LDOS calculated numerically by differentiating of I_t with respect to sample voltage.

Figure 5.8 (a) shows a 20.7 nm thick ($\sim$ 32 layers) nanosheet used investigation of the spatial doping variation. The tunneling spectra were acquired in the area marked by the dashed square. The AFM topography of this area is shown in Fig.5.8 (b). The mapping performed on 289 grid points (17 lines $\times$ 17 point)

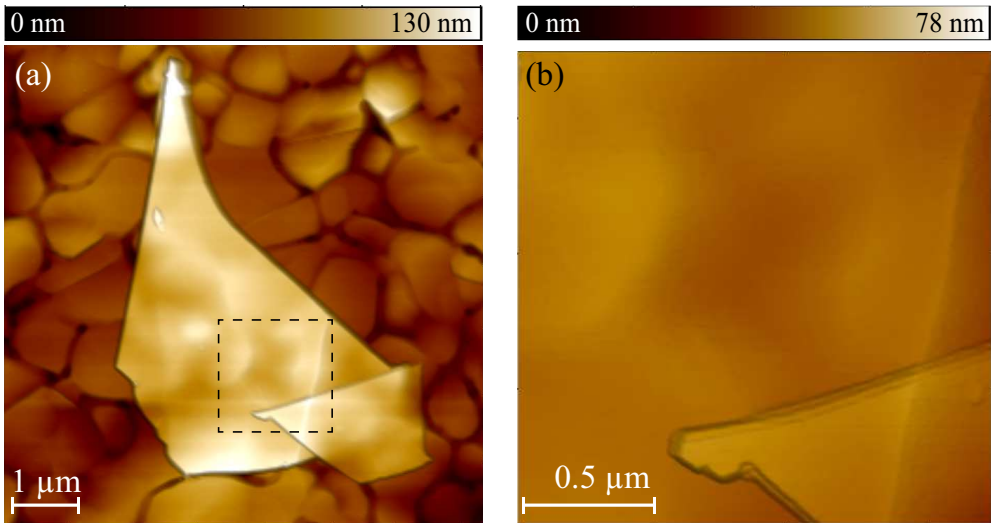

Figure 5.8: (a) AFM image of the nanosheet. (b) Zoomed AFM image of the area marked in (a)

with the resolution of $\Delta X = \Delta Y = 88$ nm.

Figure 5.9 (a) depicts the STM topography recorded simultaneously as LDOS data. The STM topography is not exactly the same as the AFM image [(Fig. 5.8 (b)] since the spectroscopy total time is about six times longer than AFM imaging. For this reason the effect of drift in X and Y directions, i.e. elongation, are more pronounced in STM topography. Figures 5.9 (b) and (c) illustrate the representative tunneling spectra obtained from the locations marked by dashed lines in Fig.**??** (a). These LDOS maps are obtained by plotting the $\mathrm{d}I/\mathrm{d}V$ curves as a function of X position and the sample voltage. The red color represents high LDOS while blue color is low LDOS. The white color pixels indicate the band onsets. The Fermi−level is marked with a white dashed line. In Fig. 5.9 (b) the E_V and E_C are located at -0.24 ± 0.11 eV and 0.47 ± 0.10 eV respectively. For Fig. 5.9 (c), $E_V = -0.29 \pm 0.12$ eV and $E_C = 0.42 \pm 0.20$ eV. The average E_V over the whole scanned area is determined to be located at -0.24 eV below Fermi−level while the average E_C is about 0.51 eV. This indicates the p−type behavior. The data shows that no change occurs in the doping type at least over an area of 1.42 × 1.42 μm^2. However, the band onsets and the bandgap show variations up to ± 0.20 eV that is more than the precision of the measurement,

i.e. $\pm$ 0.05 eV. To investigate the spatial dependency of these variations, the two-dimensional map (2D) of the LDOS, i.e. LDOS as a function of X and Y positions was obtained. Figure 5.10 represents the LDOS at the sample voltage of 0.30 V which corresponds to the energy of $E = 0.30$ eV. The bright areas indicate the high DOS. In other word, the CB has a variation in these areas. The regions with high DOS marked by circles are reproducible over few pixels in both X and Y directions. This reproducibility suggests that the variation of the bandgap might be intrinsic.

One possible reason for the variation of the bandgap is the strain induced by the substrate. It has been shown theoretically [53] that semiconductor-metal transition in MoS_2 monolayer occurs when 2D-isotropic strain is applied. Also, the reported photo-luminescence measurement on wrinkled MoS_2 nanosheets revealed that the bandgap diminishes on the wrinkles [54].

Another cause of change in the bandgap might be defects. The bandgap variation in bulk MoS_2 has been observed in a recent report[55]. The S vacancy and Mo deficient sites that can act as an electron donor and acceptor respectively were found in that sample. There is a possibility that similar defects are present in our nanosheets.

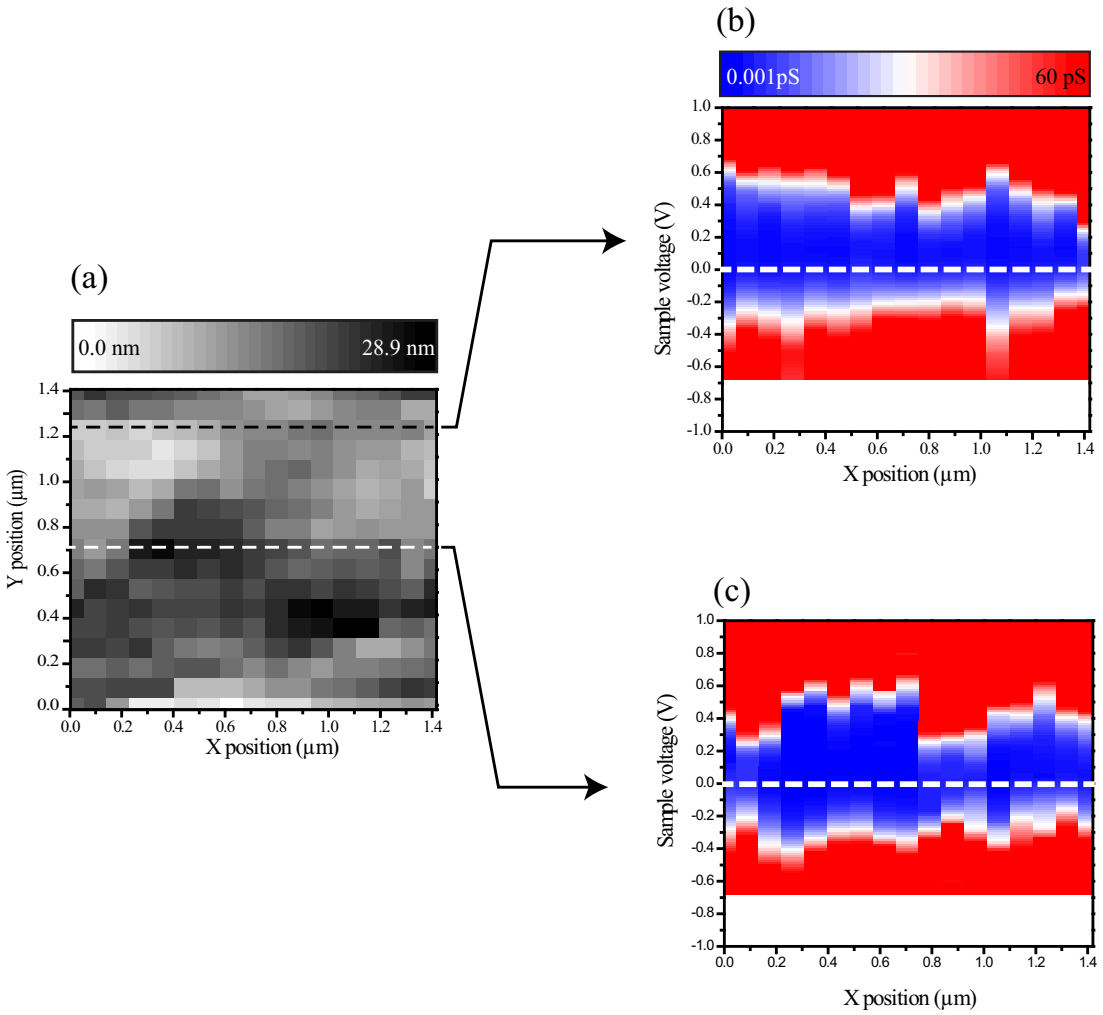

Figure 5.9: (a) The STM image taken on a area indicated in Fig. 5.8 (b). The representative LDOS maps taken along the top (b) and the lower (c) dashed lines in (a) indicating a p−type behavior. The p−typeThe stabilization current and voltage setpoints are 10 pA and -0.7 V

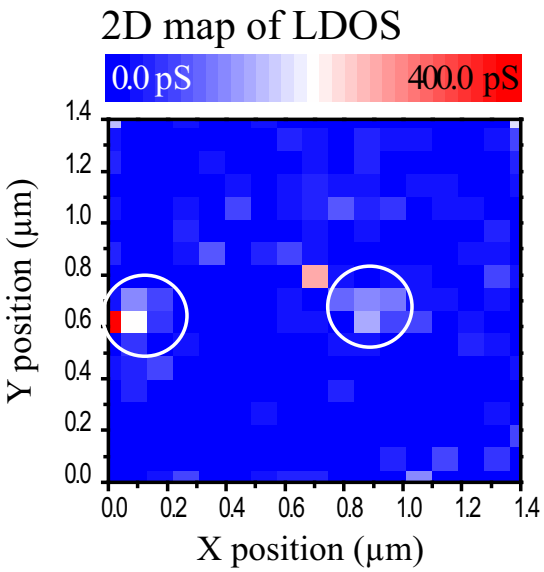

Figure 5.10: 2D map of LDOS taken in the area shown in Fig. 5.9 (a) at the energy of $E = 0.3$ eV. The bright pixels marked by the circles corresponds to the high DOS or lower CB onsets.

Chapter 6

Summary and prospectives

In summary, an atomic force microscope-assisted tunneling spectroscopy method was developed. Its performance, first demonstrated on the HOPG as a reference sample. Alternating AFM and STM measurements on this sample achieved using a Pt/Cr−coated cantilever under ambient conditions. The access to both AFM and STM signals enables us to perform AFM−assisted tunneling spectroscopy. In this method, we navigate the tip to a spot/area of interest on wide and non-atomically flat samples by AFM prior to spectroscopy. The active compensation of the vertical thermal drift for stable tunneling spectroscopy measurements, was successfully achieved using AFM feedback. AFM-assisted STS is appropriate for the study of local electronic structures on layered material devices.

The implementation of AFM−assisted STS was successfully extended to studying of local electronics properties of MoS_2 nanosheets. Point spectroscopy on different nanosheets reveals both n− and p−doping behaviours. The thickness dependence of the doping type was observed. The thinner nanosheets with the thickness less than $\sim$ 14 nm exhibit n-type while the thicker ones (thicker than $\sim$ 14 nm) show p-type behavior.

The spatial mapping of the LDOS on a p-type nanosheet reveals that the conduction type (p) does not change over an area of $\sim$ 2 μm^2. The bandgap variation was also observed in the same area. This suggests that either doping type (p or n) is dominant in individual nanosheets.

The bandgap variation was observed in 1D and 2D mapping of the LDOS. The spatial dependency of this variation, i.e. high DOS regions, suggests that this

variation might be intrinsic. We speculate two reason for the bandgap variations. One of them is the strain induced changed to the band structure due to the substrates. Second, the defects such as S and Mo vacancies might be responsible for the bandgap variations.

As for the perspectives of this work, the spatial mapping of the LDOS on several nanosheets with various thickness are desired to confirm the spatial dependency of the doping type. Furthermore, to investigate the possible originate of the dopants, such as defects, the atomically resolved STM/STS measurements using UHV/low-temperature systems is required. Moreover, the AFM-assisted STS system can be developed in order to compensate the lateral thermal drift as well. This can be accomplished by using the passive method where a constant voltage offset is added to the X and Y piezo to induce the constant movement of the piezos in the opposite direction of the drift. Therefore, stable spatial mapping will be possible even for small area of the few tens nm^2.

Appendix A

This design is to fulfil the need for a quick and clean procedure of sample mounting for AFM measurement. The typical and commercial AFM sample stages require an adhesive paste to hold the sample. For example, grease, epoxy and silver paste are common materials used for this purpose. However, they can contaminate the sample surface and hamper the replacement of the samples. To overcome the above mentioned issues, a spring-based slider can be used to hold the samples. This idea is applied in scanning electron microscopy (SEM) such as ELIONIX ELS-75005. The challenge for designing such a sample holder for AFM is the limited space between the tip/tip-holder and the sample surface and therefore the parts thickness needs to be minimized. Inspired from the design of the mentioned SEM-sample holder, I addressed the space issue by using a Si/SiO_2 wafer with the thickness of $\sim 220\mu$m as part1 (see Fig.1). The overall view of the parts is presented in Fig.1. The detail of the parts dimensions are shown in Fig.2 to Fig.4.

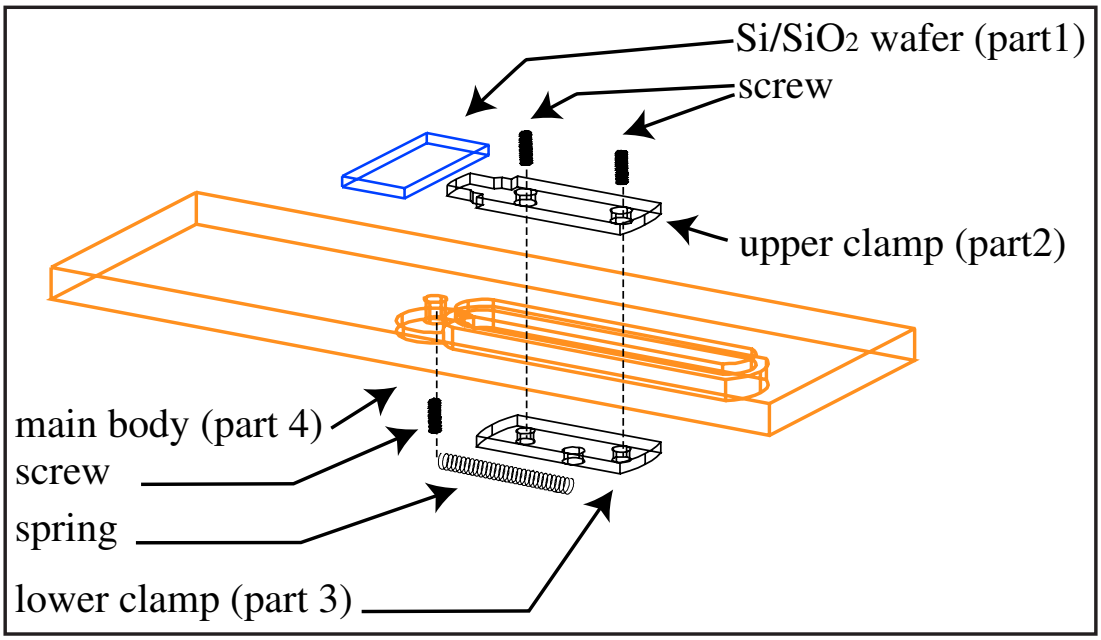

Figure 1: Design sketch of the AFM sample stage: whole parts

part2

側面図

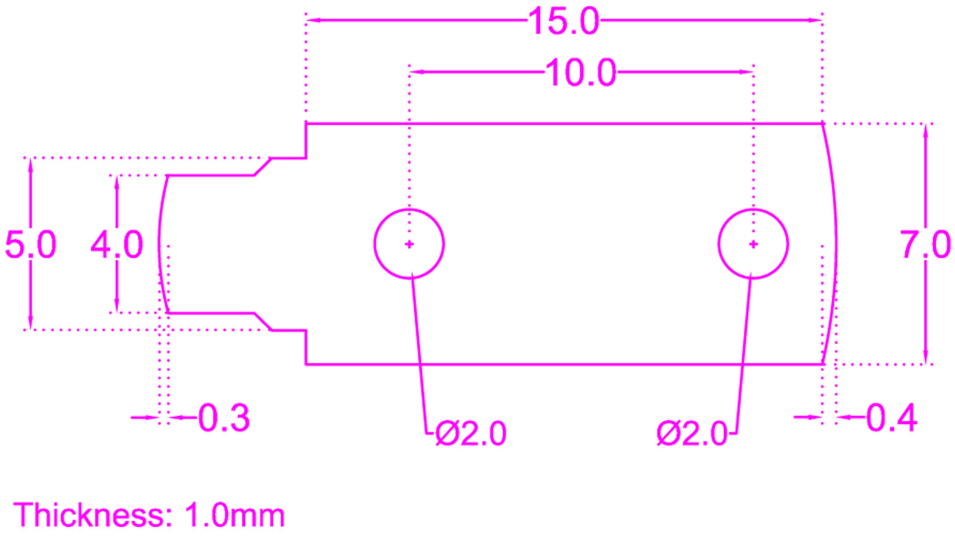

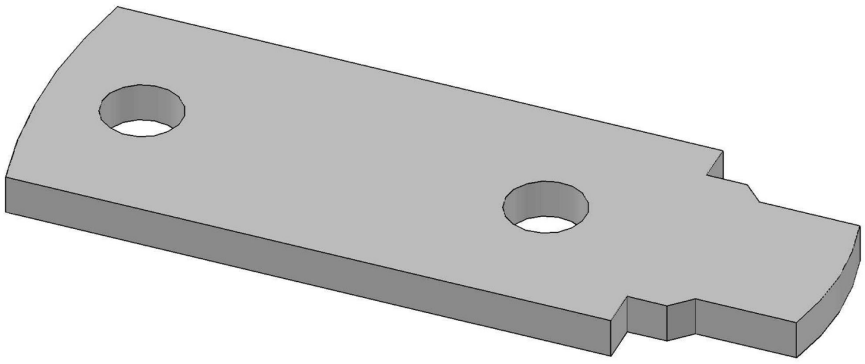

Figure 2: Design sketch of the AFM sample stage: upper clamp

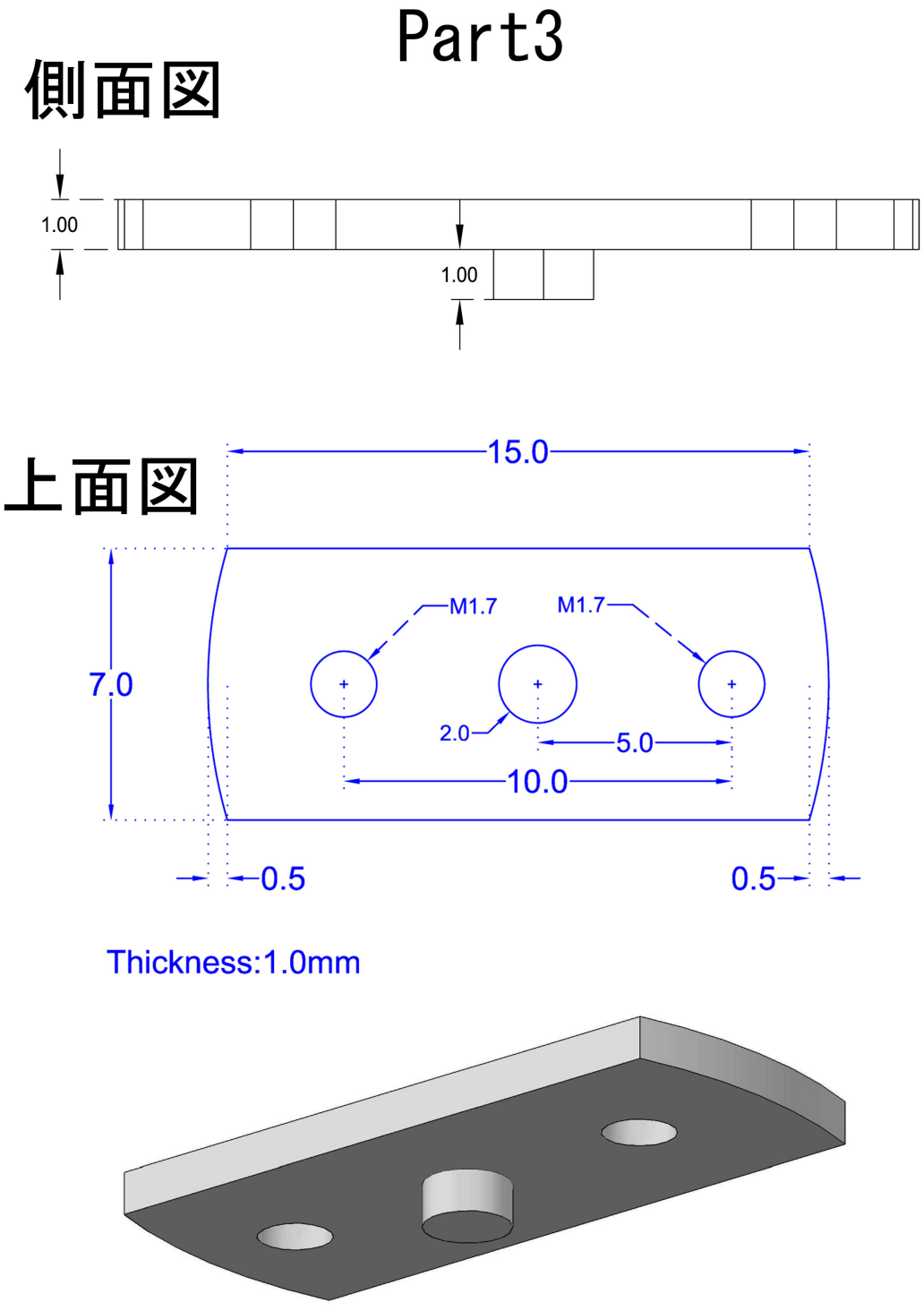

Figure 3: Design sketch of the AFM sample stage: lower clamp

Part4

側面図

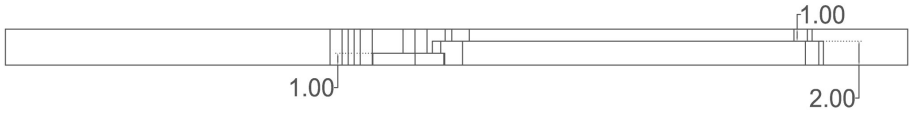

上面図

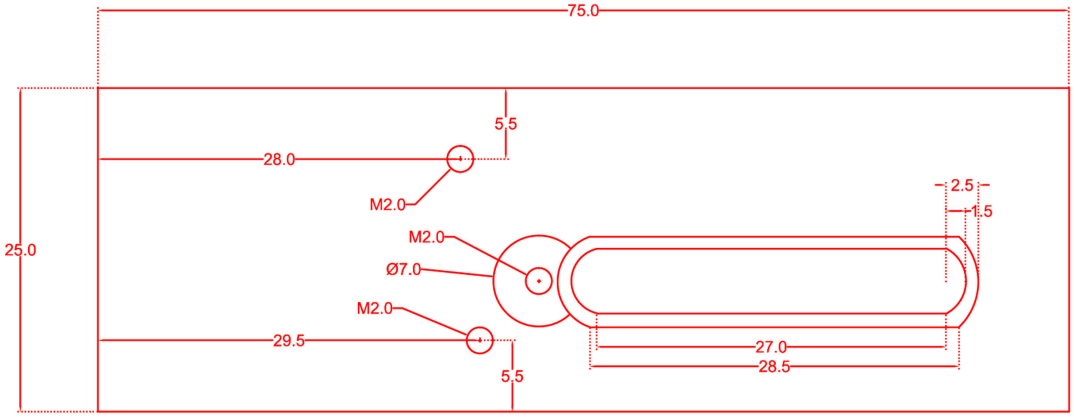

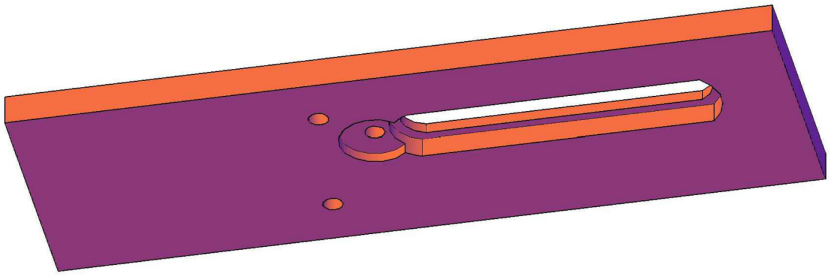

Figure 4: Design sketch of the AFM sample stage: main body

Appendix B

To use the microscope in STM mode, the following procedure files should be called from `Programming\Load User Func\` tab in IGOR: "STM.ipf", "MyXYZ.ipf, "DoIVampdata.ipf. The "STM.ipf file includes the necessary changes to use external op-amp, lock-in amplifier and a voltage source. The second file, "MyXYZ, includes the functions to control z-piezo feedback (FB) loop, and to control X/Y/Z-piezo speed in STM mode. Third file includes the codes need for controlling external sources and saving data from them. The source code are brought in the following sections.

STM Profile

The "STM.ipf file has 4 functions which override the original functions written by Asylum Reaserch with the same name. These functions set the right configuration and for sending and detecting signals to/from the external equipments. The modified source codes are as follows:

```
case "STMMeter":
if (StringMatch(XPTName,"STMMeter"))
InFastStr = "BNCIn0"
InAStr="Defl"
Copy[%FilterIn][0] = SetXPTValue(Copy,"FilterIn","Ground",SkipBit)
Copy[%InFast][0] = SetXPTValue(Copy,"InFast","BNCIn0",SkipBit)
```

```
Copy[%InA][0] = SetXPTValue(Copy,"InA","Defl",SkipBit)
Copy[%InB][0] = SetXPTValue(Copy,"InB","BNCIn1",SkipBit)
Copy[%BNCOut0][0] = SetXPTValue(Copy,"BNCOut0","BNCIn0",SkipBit)
Copy[%BNCOut1][0] = SetXPTValue(Copy,"BNCOut1","OutA",SkipBit)
Copy[%BNCOut2][0] = SetXPTValue(Copy,"BNCOut2","OutA",SkipBit)
Copy[%PogoOut][0] = SetXPTValue(Copy,"PogoOut","OutA",SkipBit)
endif

\\The following lines should be commented out:
if (ImagingMode == 4) //STM
//* CypherCopy[%InFastA][0] = SetXPTValue(CypherCopy,"InFastA",
"HolderIn0",GV("CypherXPTLock"))
//* elseif (tuneLockin == 1)

//* Copy[%FilterIn][0] = SetXPTValue(Copy,"FilterIn","Defl",SkipBit)

case "DoIV":

//* Copy[%FilterIn][0] = SetXPTValue(Copy,"FilterIn","Defl",SkipBit)
Copy[%FilterIn][0] = SetXPTValue(Copy,"FilterIn","BNCIn0",SkipBit)
Copy[%InFast][0] = SetXPTValue(Copy,"InFast","FilterOut",SkipBit)
Copy[%InA][0] = SetXPTValue(Copy,"InA","BNCIn1",SkipBit)
Copy[%Shake][0] = SetXPTValue(Copy,"Shake","Ground",SkipBit)
Copy[%BNCOut0][0] = SetXPTValue(Copy,"BNCOut0","FilterOut",SkipBit)
```

```
case 4: //STM
Copy[%InFast][0] = SetXPTValue(Copy,"InFast","BNCIn0",SkipBit)
Copy[%FilterIn][0] = SetXPTValue(Copy,"FilterIn","Ground",
SkipBit)
//* Copy[%InFast][0] = SetXPTValue(Copy,"InFast","FilterOut",
SkipBit)
//* Copy[%FilterIn][0] = SetXPTValue(Copy,"FilterIn","BNCIn0",
SkipBit)
Copy[%InA][0] = SetXPTValue(Copy,"InA","Defl",SkipBit)
Copy[%InB][0] = SetXPTValue(Copy,"InB","BNCIn1",SkipBit)
```

In the function "ARGetImagingMode(InfoStruct, [ImagingMode])" the following codes need to be changed:

```
\\* The signs of the gain parameters are changed as follows:
case 4: //STM
GainSign =- Sign(SurfaceVoltage)
SetpointParm = "CurrentSetpointVolts"
Wave InfoStruct.SetpointVarWave = MVW
Input = "Current"
if (SafeGVByLabel(MVW,"LogFeedback",ColumnStr="Value",NotThereValue
=1)) Input = "Log.Output"
endif
Setpoint = (InfoStruct.SetpointVarWave[%$SetpointParm][0]*MVW
[%OrcaGain][0]*-GainSign-ARDoIV[%OrcaOffset][0]*cOrcaOffsetSign)/
MVW[%OrcaGain][0]
```

```
IScale *=.1*Sign(SurfaceVoltage)
PScale *=.1*Sign(SurfaceVoltage)
if (StringMatch(Input,"Log.Output"))
Setpoint = (InfoStruct.SetpointVarWave[%$SetpointParm][0]*MVW[%Orca
Gain][0]*-GainSign)/MVW[%OrcaGain][0]
Setpoint = GetLogValue("Current",Setpoint)
PScale *= 1
IScale *=1
SScale *= .1*Sign(SurfaceVoltage)
Endif

//* Feedback.PGain = PGain*PScale*GainSign
//* Feedback.IGain = IGain*IScale*GainSign
//* Feedback.SGain = SGain*SScale*GainSign
//* Feedback.DGain = DGain*DScale*GainSign
```

In the "Writebias" function;

```
if ((ImagingMode == 4) || (SurfaceVoltageParms & 2) ||
(WhichListItem("Current",ImageChannelList) > -1) || (WhichListItem
("Current2",ImageChannelList) > -1) || ((NapVoltageParms & 0x2000) &&
 NapMode))
//* SurfaceParm = "SurfaceVoltage"
SurfaceXPT = "OutC"
ShakeXPT = "Ground"
```

In the "AdjustScanXPT()" function:

```
case 4: //STM //not sure if this works here, but lets try it.
//* if (! IsCypher) //if you are NOT on Cypher
//then we use the filters on Current
Copy[%FilterIn][0] = SetXPTValue(Copy,"FilterIn","Ground",SkipBit)
Copy[%InFast][0] = SetXPTValue(Copy,"InFast","BNCIn0",SkipBit)
Copy[%InA][0] = SetXPTValue(Copy,"InA","Defl",SkipBit)
Copy[%InB][0] = SetXPTValue(Copy,"InB","BNCIn1",SkipBit)
Copy[%BNCOut0][0] = SetXPTValue(Copy,"BNCOut0","BNCIn0",SkipBit)
Copy[%BNCOut1][0] = SetXPTValue(Copy,"BNCOut1","OutA",SkipBit)
Copy[%BNCOut2][0] = SetXPTValue(Copy,"BNCOut2","OutA",SkipBit)
Copy[%PogoOut][0] = SetXPTValue(Copy,"PogoOut","OutA",SkipBit)
//*
ImageChannelList = RemoveFromList("Current",ImageChannelList)
aDCList = RemoveFromList("InFast",aDCList)
//* else
//* if (WhichListItem("Deflection",ImageChannelList,";",0,0) > -1)
//* hookUpDeflection = 1
//* ImageChannelList = RemoveFromList("Deflection",ImageChannelList)
//* endif
//* endif
break
case"Scan":
if ((ImagingMode == 4) || (SurfaceVoltageParms & 2) ||
(WhichListItem("Current",ImageChannelList) > -1) ||
(WhichListItem("Current2",ImageChannelList) > -1) ||
```

```
((NapVoltageParms & 0x2000) && NapMode))
//* SurfaceParm = "SurfaceVoltage"
SurfaceXPT = "OutC"
ShakeXPT = "Ground"
case"Meter":
ShakeXPT = "Ground"
BNCOut0XPT = "FilterOut"
BNCOut1XPT = "OutC"
```

Z-piezo Feedback control: AFM-FB in repulsive regime

The procedure file (MyXYZ) was written for controlling the piezo-voltage ramping rate ,i.e.the speed.

```
Function repFFB()
Struct ARFeedbackStruct FB
String ErrorStr = ""
ARGetFeedbackParms(FB,"Height")
FB.Input =  "Input.A"
FB.Setpoint=td_readvalue("Deflection")
FB.IGain=700
FB.PGain=0.00
FB.StartEvent = "Always"
FB.StopEvent = "Never"
ErrorStr += ir_writePIDSloop(FB)
ErrorStr += num2str(td_WriteString("Event."+FB.StartEvent,"Once"))+"
," ARREportError(ErrorStr)
```

```
End  //repFFB()
```

Controlling X-Ypiezo speed for 1D and 2D spectroscopy

The dX and dY in the arguments are the X and Y steps in nanometer for LDOS mapping.

```
Function MyNudgerX(dX)
Variable dX
Variable Xstepsize=abs(dX)*1e-9
ARSetVarFunc("NudgerStepSizeSetVar_0",Xstepsize,"",
"ARcustumVAriablesWave[%NudgerStepSize]")
if (dX>0)
ARExecuteControl("XUp","Nudger",0,"")
else
ARExecuteControl("XDown","Nudger",0,"")
endif
End //MyNudger(dX)
Function MyNudgerY(dY)
Variable dY
Variable Ystepsize=abs(dY)*1e-9
ARSetVarFunc("NudgerStepSizeSetVar_0",Ystepsize,"",
"ARcustumVAriablesWave[%NudgerStepSize]")
if (dY>0)
ARExecuteControl("YUp","Nudger",0,"")
else
ARExecuteControl("YDown","Nudger",0,"")
endif
```

```
End //MyNudger(dY)
```

Tip-Approach-Speed Control for STM

This function is necessary for STM since the default speed of tip approaching is set to be proportional to the gain parameters which makes a fast approach in STM mode specially when the feedback is in logarithmic mode. The function have two arguments. First is the approach speed in nm/s and second is the current setpoint in Volt.

```
Function MyEngage(speed,setpoint)

variable speed,setpoint

// speed in nm/s

Make/T/O/N=0 Root:CTFC

Wave/T CTFC = Root:CTFC

Variable Error = 0

td_ReadGroup("CTFC",CTFC)

Variable maxApproachDistVolts = td_RV("Z%Output") - (-9)

variable slope1 = speed *(1e-9) /td_readvalue("ZLVDTsens")

CTFC[%RampChannel] = "Output.Z"

CTFC[%RampOffset1] = num2str(maxApproachDistVolts)

CTFC[%RampSlope1] = num2str( slope1 )

CTFC[%RampOffset2] = "0"

CTFC[%RampSlope2] = "0"

CTFC[%TriggerChannel1] = "Input.Fast"

CTFC[%TriggerValue1] =  num2str(-setpoint)

//wait for Current to be > setpoint).

CTFC[%TriggerCompare1] = "<="

CTFC[%TriggerChannel2] = "Dummy%output"
```

```
CTFC[%DwellTime1] = "0"
CTFC[%DwellTime2] = "0"
CTFC[%Callback] = "logFB()"
CTFC[%EventDwell] = "4"
CTFC[%EventRamp] = "3"
CTFC[%EventEnable] = "0"
td_stop()
Error += td_WriteValue("Dummy%Output",-10)
Error += td_writeGroup("CTFC",CTFC)
Error += td_WriteString("0%Event","Once")
if (Error)
Print "Error: "+num2str(Error)+" in: "+GetFuncname()
DoWindow/H
endif
End //MyEngage
```

Saving the Data From External Sources

The file procedure (DoIVampdata)includes the necessary changes for this part. In the function "ARDoIVDitherCallback(DoneTheBiasRamp)", the bellow codes should be modified in order to send, receive and save signals to/from lock-in amplifier and the op-amp.

```
Wave Current = InitOrDefaultWave(DataFolder+"Current",0)
Wave Current2 = InitOrDefaultWave(DataFolder+"Current2",0)
Wave Defl = InitOrDefaultWave(DataFolder+"Defl",0)
Wave Raw = InitOrDefaultWave(DataFolder+"Raw",0)
//*   Wave XSensor = InitOrDefaultWave(DataFolder+"XSensor",0)
//* Wave YSensor = InitOrDefaultWave(DataFolder+"YSensor",0)
```

```
Wave ZSensor = InitOrDefaultWave(DataFolder+"ZSensor",0)
Wave ZOutput = InitOrDefaultWave(DataFolder+"ZOutput",0)
Wave ZOutputV = InitOrDefaultWave(DataFolder+"ZOutputV",0)
Wave BiasWave = InitOrDefaultWave(DataFolder+"Bias",0)
//* Wave AmplitudeV = InitOrDefaultWave(DataFolder+"AmplitudeV",0)
Wave UserIn1 = InitOrDefaultWave(DataFolder+"UserIn1",0)
//* Wave Amplitude2V = InitOrDefaultWave(DataFolder+"Amplitude2V",0)
//* Wave Phase = InitOrDefaultWave(DataFolder+"Phase",0)
//* Wave Phase2 = InitOrDefaultWave(DataFolder+"Phase2",0)
ErrorStr += IR_xSetOutWave(0,cDoIVEvent,OutPutDAC,DriveWave,
num2char(7),ARGetDeci(-1/DimDelta(DriveWave,0))) //version 12
String InputADC = "Current"
//* ErrorStr += IR_XSetInWave(2,"0",InputADC,Current,
"ARDoIVCallback()",Decimation)
ErrorStr += IR_XSetInWavePair(2,cDoIVEvent,InputADC,Current,
"Deflection",Defl,"ARDoIVCallback()",Decimation)//*version12
//* ErrorStr += IR_XSetInWavePair(0,"0","ZSensor",Raw,"Input.A",
UserIn1,"ARDoIVCallback()",Decimation) //*version11
IR_XSetInWavePair(0,cDoIVEvent,"ZSensor",Raw,"Input.B",UserIn1,"",
Decimation)                    //*version12
ErrorStr += IR_XSetInWave(1,"0",OutputDAC,BiasWave,"",-Decimation)
ErrorStr += IR_XSetInWave(1,cDoIVEvent,OutputDAC,BiasWave,"",
-Decimation)      //*version12
```

To save the signals in ASCII format and display them in DoIV panel the function "ARDoIVCallback()" changed as follows:

```
String DataFolder = GetDF("DoIV")
Wave DriveWave = $DataFolder+"DriveWave"
Wave Raw = $DataFolder+"Raw"
Wave ZSensor = $DataFolder+"ZSensor"
Wave Current = $DataFolder+"Current"
Wave Current2 = $DataFolder+"Current2"
Wave Defl = $DataFolder+"Defl"
Wave ZOutput = $DataFolder+"ZOutput"
Wave ZOutputV = $DataFolder+"ZOutputV"
Wave BiasWave = $DataFolder+"Bias"
Wave UserIn1 = $DataFolder+"UserIn1"
String DataTypes = "Bias;Cur;ZSnsr;In1;"
Save/G/O/J/P=$PName Data2Disk as NameOfWave(Data2Disk)+".txt"
Current=-Current \\*change the sign of current
FastOp BiasWave = (-BiasOffset)+1.9354*BiasWave
\\*scale the voltage bias to use external function generator.
```

Appendix C

PUBLICATIONS & PRESENTATIONS

1. A. Vakhshouri, K. Hashimoto and Y. Hirayama, "Atomic force microscope-assisted scanning tunneling spectroscopy in ambient conditions", *Microscopy*, 63, 475-479, 2014.

2. K. Snoussi, A. Vakhshouri, H. Okimoto, T. Takenobu, Y. Iwasa, S.Maruyama, K. Hashimoto and Y. Hirayama, "Electrical transport properties in a single-walled carbon nanotube network", *Phys. Status Solidi C 9*, 183-186, 2012.

3. A. Vakhshouri, K. Nagase, K. Hashimoto and Y. Hirayama, "Layer-Thinning of MoS_2 Using Electron Beam and Atomic Force Microscope", The 40th International Symposium on Compound Semiconductors (ISCS) (Poster presentation), Kobe, Japan, 2013.

4. A. Vakhshouri, K. Nagase, K. Hashimoto and Y. Hirayama, "Layer-Thinning of MoS_2 Using Electron Beam and Atomic Force Microscope", The 60th Japan Society of Applied Physics (JSAP) spring meeting, Kanagawa, Japan, 2013.

5. A. Vakhshouri, K. Hashimoto and Y. Hirayama, "Scanning tunneling microscopy of electronic properties of bulk and layered MoS_2", The 4th Global COE international Symposium, Sendai, Japan, 2012.

6. A. Vakhshouri, K. Snoussi, K. Hashimoto and Y. Hirayama, "Transport properties of carbon nanotube network in magnetic field", Quantum Information Process Projects, Yatsugatake, Japan, 2011.

References

[1] K. S. Novoselov et al. “Electric field effect in atomically thin carbon films”. In: *Science* 306.5696 (2004), pp. 666–669. DOI: 10.1126/science.1102896.

[2] KF Mak et al. “Atomically Thin MoS2: A New Direct-Gap Semiconductor”. In: *Physical Review Letters* 105.13 (2010). DOI: 10.1103/PhysRevLett.105.136805.

[3] B Radisavljevic et al. “Single-layer MoS2 transistors”. In: *Nature nanotechnology* 6.3 (2011), pp. 147–150.

[4] Saptarshi Das et al. “High performance multilayer MoS2 transistors with scandium contacts”. In: *Nano letters* 13.1 (2012), pp. 100–105.

[5] Xiaolin Li et al. “Chemically Derived, Ultrasmooth Graphene Nanoribbon Semiconductors”. In: *Science* 319.5867 (2008), pp. 1229–1232. DOI: 10.1126/science.1150878. eprint: http://www.sciencemag.org/content/319/5867/1229.full.pdf.

[6] G. Binnig et al. “Tunneling through a controllable vacuum gap”. In: *Applied Physics Letters* 40.2 (1982), pp. 178–180. DOI: http://dx.doi.org/10.1063/1.92999.

[7] Kin Fai Mak et al. “Atomically thin MoS 2: a new direct-gap semiconductor”. In: *Physical Review Letters* 105.13 (2010), p. 136805.

[8] Y Martin, CC WILLIAMS, and HK WICKRAMASINGHE. “ATOMIC FORCE MICROSCOPE FORCE MAPPING AND PROFILING ON A SUB 100-A SCALE”. In: *Journal of Applied Physics* 61.10 (1987), pp. 4723–4729. DOI: 10.1063/1.338807.

[9] Seizo Morita, Yasuhiro Sugawara, and Yoshinobu Fukano. "Atomic force microscope combined with scanning tunneling microscope [AFM/STM]". In: *Japanese journal of applied physics* 32.6S (1993), p. 2983.

[10] S Hembacher et al. "Local spectroscopy and atomic imaging of tunneling current, forces, and dissipation on graphite". In: *Physical Review Letters* 94.5 (2005). DOI: 10.1103/PhysRevLett.94.056101.

[11] Masayuki Abe et al. "Drift-compensated data acquisition performed at room temperature with frequency modulation atomic force microscopy". In: *Applied Physics Letters* 90.20, 203103 (2007), pp. –. DOI: http://dx.doi.org/10.1063/1.2739410.

[12] Sunkook Kim et al. "High-mobility and low-power thin-film transistors based on multilayer MoS2 crystals". In: *Nature communications* 3 (2012), p. 1011.

[13] Britton WH Baugher et al. "Intrinsic Electronic Transport Properties of High-Quality Monolayer and Bilayer MoS2". In: *Nano letters* 13.9 (2013), pp. 4212–4216.

[14] Marcio Fontana et al. "Electron-hole transport and photovoltaic effect in gated MoS2 Schottky junctions". In: *Scientific reports* 3 (2013).

[15] Dmitri Golberg. "Nanomaterials: exfoliating the inorganics". In: *Nature nanotechnology* 6.4 (2011), pp. 200–201.

[16] Eugene S Kadantsev and Pawel Hawrylak. "Electronic structure of a single MoS_2 monolayer". In: *Solid State Communications* 152.10 (2012), pp. 909–913.

[17] Andrea Splendiani et al. "Emerging Photoluminescence in Monolayer MoS2". In: *Nano Letters* 10.4 (2010). PMID: 20229981, pp. 1271–1275. DOI: 10.1021/nl903868w. eprint: http://dx.doi.org/10.1021/nl903868w.

[18] G. Binnig and H. Rohrer. "SCANNING TUNNELING MICROSCOPY". In: *Helvetica Physica Acta* 55.6 (1982), pp. 726–735.

[19] Roland Wiesendanger. *Scanning Probe Microscopy and Spectroscopy*. Cambridge Books Online. Cambridge University Press, 1994.

[20] Joseph A Stroscio and William J Kaiser. *Scanning tunneling microscopy*. Vol. 27. Academic Press, 1993.

[21] J. Bardeen. "Tunnelling from a Many-Particle Point of View". In: *Phys. Rev. Lett.* 6 (2 1961), pp. 57–59. DOI: 10.1103/PhysRevLett.6.57.

[22] G. Binnig, C. F. Quate, and Ch. Gerber. "Atomic Force Microscope". In: *Phys. Rev. Lett.* 56 (9 1986), pp. 930–933. DOI: 10.1103/PhysRevLett.56.930.

[23] Gerhard Meyer and Nabil M Amer. "Novel optical approach to atomic force microscopy". In: *Applied physics letters* 53.12 (1988), pp. 1045–1047.

[24] T. R. Albrecht et al. "Frequency modulation detection using high cantilevers for enhanced force microscope sensitivity". In: *Journal of Applied Physics* 69.2 (1991), pp. 668–673. DOI: http://dx.doi.org/10.1063/1.347347.

[25] Franz J Giessibl. "Atomic resolution of the silicon (111)-(7x7) surface by atomic force microscopy". In: *Science* 267.5194 (1995), pp. 68–71.

[26] Hans-Jürgen Butt, Brunero Cappella, and Michael Kappl. "Force measurements with the atomic force microscope: Technique, interpretation and applications". In: *Surface science reports* 59.1 (2005), pp. 1–152.

[27] Yasuhiro Sugawara et al. "Simultaneous observation of atomically resolved AFM/STM images of a graphite surface". In: *Japanese journal of applied physics* 29.1A (1990), p. L157.

[28] Seizo Morita, Roland Wiesendanger, and Ernst Meyer. *Noncontact atomic force microscopy*. Vol. 1. Springer, 2002.

[29] Ke Xu, Peigen Cao, and James R. Heath. "Scanning Tunneling Microscopy Characterization of the Electrical Properties of Wrinkles in Exfoliated Graphene Monolayers". In: *Nano Letters* 9.12 (2009). PMID: 19852488, pp. 4446–4451. DOI: 10.1021/nl902729p. eprint: http://dx.doi.org/10.1021/nl902729p.

[30] Guohong Li, Adina Luican, and Eva Y. Andrei. "Self-navigation of a scanning tunneling microscope tip toward a micron-sized graphene sample". In: *Review of Scientific Instruments* 82.7, 073701 (2011), pp. –. DOI: http://dx.doi.org/10.1063/1.3605664.

[31] Adina Luican-Mayer. "Scanning tunneling microscopy and spectroscopy studies of graphene". PhD thesis. Graduate School—new Brunswick Rutgers, The State University Of New Jersey, 2012.

[32] CR Dean et al. "Boron nitride substrates for high-quality graphene electronics". In: *Nature nanotechnology* 5.10 (2010), pp. 722–726.

[33] D.R. Lide. *CRC Handbook of Chemistry and Physics, 84th Edition*. CRC HANDBOOK OF CHEMISTRY AND PHYSICS. Taylor & Francis, 2003.

[34] Amin Vakhshouri, Katsushi Hashimoto, and Yoshiro Hirayama. "Atomic force microscope-assisted scanning tunneling spectroscopy under ambient conditions". In: *Microscopy* 63.6 (2014), pp. 475–479. DOI: 10.1093/jmicro/dfu028. eprint: http://jmicro.oxfordjournals.org/content/63/6/475.full.pdf+html.

[35] J. L. Hutter and J. Bechhoefer. "CALIBRATION OF ATOMIC-FORCE MICROSCOPE TIPS". In: *Review of Scientific Instruments* 64.7 (1993), pp. 1868–1873. DOI: 10.1063/1.1143970.

[36] C. M. Mate et al. "DIRECT MEASUREMENT OF FORCES DURING SCANNING TUNNELING MICROSCOPE IMAGING OF GRAPHITE". In: *Surface Science* 208.3 (1989), pp. 473–486. DOI: 10.1016/0039-6028(89)90014-9.

[37] Y Sugawara, T Ishizaka, and S Morita. "ORIGIN OF ANOMALOUS CORRUGATION HEIGHT OF STM IMAGES OF GRAPHITE". In: *Japanese Journal of Applied Physics Part 1-Regular Papers Short Notes & Review Papers* 29.8 (1990), pp. 1533–1538. DOI: 10.1143/JJAP.29.1533.

[38] Y. Sugawara, T. Ishizaka, and S. Morita. "SCANNING FORCE TUNNELING MICROSCOPY OF A GRAPHITE SURFACE IN AIR". In: *Journal of Vacuum Science & Technology B* 9.2 (1991), pp. 1092–1095. DOI: 10.1116/1.585267.

[39] S. C. Meepagala, F. Real, and C. B. Reyes. "TIP-SAMPLE INTERACTION FORCES IN SCANNING TUNNELING MICROSCOPY - EFFECTS OF CONTAMINANTS". In: *Journal of Vacuum Science & Technology B* 9.2 (1991), pp. 1340–1342. DOI: 10.1116/1.585192.

[40] Y. Suganuma and A. Dhirani. "A hybrid scanning tunneling-atomic force microscope operable in air". In: *Review of Scientific Instruments* 74.10 (2003), pp. 4373–4377. DOI: 10.1063/1.1610784.

[41] P. J. de Pablo et al. "Mechanical and electrical properties of nanosized contacts on single-walled carbon nanotubes". In: *Advanced Materials* 12.8 (2000), pp. 573–576. DOI: 10.1002/(sici)1521-4095(200004)12:8<573::aid-adma573>3.0.co;2-3.

[42] H. J. Mamin et al. "CONTAMINATION-MEDIATED DEFORMATION OF GRAPHITE BY THE SCANNING TUNNELING MICROSCOPE". In: *Physical Review B* 34.12 (1986), pp. 9015–9018. DOI: 10.1103/PhysRevB.34.9015.

[43] R. Proksch, J. Cleveland, and D. Bocek. *Linear variable differential transformers for high precision position measurements*. Generic. 2006.

[44] Y. Niimi et al. "Scanning tunneling microscopy and spectroscopy of the electronic local density of states of graphite surfaces near monoatomic step edges". In: *Physical Review B* 73.8 (2006), p. 8. DOI: 10.1103/PhysRevB.73.085421.

[45] Andrea Liscio et al. "Tip-Sample Interactions in Kelvin Probe Force Microscopy: Quantitative Measurement of the Local Surface Potential". In: *Journal of Physical Chemistry C* 112.44 (2008), pp. 17368–17377. DOI: 10.1021/jp806657k.

[46] M. Salmeron et al. "TIP-SURFACE FORCES DURING IMAGING BY SCANNING TUNNELING MICROSCOPY". In: *Journal of Vacuum Science & Technology B* 9.2 (1991), pp. 1347–1352. DOI: 10.1116/1.585194.

[47] Randall M Feenstra and Joseph A Stroscio. "Tunneling spectroscopy of the GaAs (110) surface". In: *Journal of Vacuum Science & Technology B* 5.4 (1987), pp. 923–929.

[48] RM Feenstra. "Tunneling spectroscopy of the (110) surface of direct-gap III-V semiconductors". In: *Physical Review B* 50.7 (1994), p. 4561.

[49] SC Meepagala and F Real. "Detailed experimental investigation of the barrier-height lowering and the tip-sample force gradient during STM operation in air". In: *Physical Review B* 49.15 (1994), p. 10761.

[50] C Julian Chen. *Introduction to scanning tunneling microscopy*. Vol. 227. Oxford University Press New York, 1993.

[51] PJ Kowalczyk. "Investigation of STM tip influence on the recorded position of the Shockley surface state on Au (111)". In: *Surface Science* 603.5 (2009), pp. 747–751.

[52] Wenzhong Bao et al. "High mobility ambipolar MoS2 field-effect transistors: Substrate and dielectric effects". In: *Applied Physics Letters* 102.4 (2013), p. 042104.

[53] Mahdi Ghorbani-Asl et al. "Strain-dependent modulation of conductivity in single-layer transition-metal dichalcogenides". In: *Physical Review B* 87.23 (2013), p. 235434.

[54] Andres Castellanos-Gomez et al. "Local strain engineering in atomically thin MoS2". In: *Nano letters* 13.11 (2013), pp. 5361–5366.

[55] Stephen McDonnell et al. "Defect-Dominated Doping and Contact Resistance in MoS2". In: *ACS nano* 8.3 (2014), pp. 2880–2888.